UNIVERSITY OF TECHNOLOGY SYDNEY
Faculty of Engineering and Information Technology

Heartbeat Detection with complicated Noises Using FMCW Radar

by

Jingwei Liu

A Thesis Submitted
in Partial Fulfillment of the
Requirements for the Degree

Master of Research

Sydney, Australia

2021

Certificate of Authorship/Originality

I, Jingwei Liu declare that this thesis, is submitted in fulfilment of the requirements for the award of Master of Computer Science, in the FEIT at the University of Technology Sydney.

This thesis is wholly my own work unless otherwise referenced or acknowledged. In addition, I certify that all information sources and literature used are indicated in the thesis.

This document has not been submitted for qualifications at any other academic institution.

This research is supported by the Australian Government Research Training Program.

Signature: Production Note: Signature removed prior to publication.

Date:22/1/2021

ABSTRACT

Heartbeat Detection with complicated Noises Using FMCW Radar

by

Jingwei Liu

Remote heartbeat detection is particular useful for applications in smart home, digital health, and disaster relief (e.g. earthquakes) because of its ability to conduct accurate monitoring of heartbeats at a long distance. The millimeter wave band is of great sig-nificance for remote heartbeat detection, and the millimeter wave-based frequency modulated continuous radar (FMCW) radar is an excellent device for remote heartbeat detection. In the research of radar-based heartbeat detection, an important problem is the interference of human motion in the signal. Artifacts caused by motion appear across all frequency bands, thereby polluting the true heartbeat waveforms. Therefore, removing random body motion (RBM)'s interference to heartbeat detection has become the most challenging task at present. In this thesis, the heartbeat detection technology based on FMCW radar is studied and contributions to the research of the following two issues is made:

1. In heartbeat detection, greatly reduce the interference of motion artifacts and background noise when using the sparsity difference to extract the heartbeat waveform.

2. The subject's small degree of random movement (upper body movement, lower body static) caused greater interference.

For the first question, we use convolutional sparse coding (CSC) to replace the sparse coding (SC) in the previous work. In order to simulate complex phase noise and motion artifacts, we use gaussian mixture model (GMM) to model the noise. When solving the CSC problem, in order to speed up the entire process, we use (non-convex inexact accelerated proximal gradient)niAPG to achieve rapid decline. Simulations and experiments verify the effectiveness of our method. For the second question,

we added an additional clustering step to the ordinary decomposition algorithm, and proposed new parameters to improve the accuracy of clustering. We extract the initial static data as the initial input, and compare the data of two adjacent time windows to extract the peak heartbeat. For the task of extracting the heartbeat from the target of the upper body motion (large range of random motion), our method proved effective.

Dedication

To my parents Yin Xu and Shengxi Liu.

Acknowledgements

First and foremost, I would like to extend my deepest gratitude to my principal professor Andrew. J. Zhang. His patience and enlightening instruction allowed me to see who a real professor is. Without his teachings, I would not have finished this thesis. I also extend my thanks to Professor Richard Xu. His professionalism and work attitude impressed me deeply. I also thank my parents. Finally, I' d like to thank all my friends, especially Chunrui Liu, Zhengguo Shi, and Andre Pearce. Thank you for your guidance and help.

Jingwei Liu

Sydney, Australia, 2021.

List of Publications

Conference Papers

Jingwei Liu, and J.Andrew.Zhang, "Gaussian Mixture Model based Convolutional Sparse Coding for Radar Heartbeat Detection," *Proc. IEEE Int. Conf. on ICSPCS*, Dec. 14-16, 2020.

Contents

List of Figures

Abbreviation

APG - Accelerated Proximal Gradient

BSS - Blind Source Separation

CSC - Convolutional Sparse Coding

ECG - Electrocardiography

EM - Expectation Maximization

EMD - Empirical Mode Decomposition

FMCW - Frequency Modulated Continuous Wave

ICA - Independent Component Analysis

GMM - Gaussian Mixture Model

IF - Intermediate Frequency

LO - Local Oscillator(In some down-convert process, LO signal can betreated as transmitted signal)

MIMO - Multi input multi output

MA - Motion Artifact

PPG - Photoplethysmography

RBM- Random Body Movement

RMSE - Root Means Square error

RSM - Random System Movement

SHSC - Second Harmonic Signal Component

SSA - Singular Spectrum Analysis

Nomenclature and Notation

Capital letters denote matrices.

Lower-case alphabets denote column vectors.

$(.)^T$ denotes the transpose operation.

I_n is the identity matrix of dimension $n \times n$.

0_n is the zero matrix of dimension $n \times n$.

$\mathbb{R}$, $\mathbb{R}^+$ denote the field of real numbers, and the set of positive reals, respectively.

Chapter 1

Introduction

This chapter briefly reviews the human activity recognition backgrounds using an FMCW radar and the up-to-date development of this technique in the literature. The research objectives are expressed in the following section, and the structure is outlined at the end of this chapter.

1.1 Background of Human Activity Recognition

One of the essential parameters evaluating individual health conditions, the heartbeat, can be detected by capturing the chest and hand's blood vessel vibration. Tying thin wires to hands is the prototype of modern electrocardiography. Modern electrocardiograms (ECG) can capture the heartbeat with sufficient accuracy.

The critical parameters for evaluating individual health with ECG are heart rate, the shape of the QRS (Q wave, R wave, and S wave in ECG) wave shape, and the amplitude of the QRS wave. Obtaining information on the latter two parameters requires much prior knowledge, which only experienced doctors can provide. Some unsupervised learning algorithms (clustering) have been used to separate ECG with (or no) health risks in the last ten years. These methods will save much labor and time costs for disease diagnosis and health detection, but long-term health monitoring implies that the input time series will be considerably longer. Therefore, heart rate and its changes have become more critical parameters, and many health detection applications only use heart rate as an evaluation parameter.

In addition to ECG, another contact-type heart rate acquisition method is photoplethysmography (PPG) signal. The infusion of blood into the dermis and subcuta-

neous tissues can be captured and converted into PPG. Heart rate information can be extracted from PPG, which can be obtained from human fingers. The human body does not need to remain still, which implies that PPG can be obtained from a portable device on a moving person. This method's predominant problem is that the random motion of the human body and the random movement of the system will produce artifacts and interfere with the accuracy of the heart rate recognition. One of the best ways to resolve this problem is to capture the velocity (acceleration) of the movement and use it to compensate for the receive signal.

In recent years, in addition to contact-based heart-rate collection methods, non-contact heart-rate detection received increased attention. Compared to traditional contact-based detection, although the accuracy is lower, non-contact capture offers the following advantages: 1. It can detect objects that are hard to locate, such as people buried under ruins after an earthquake, and is used for imaging objects that should not be touched, such as severely burned skin that cannot be touched with an electrode. 2. The scope of application is broader, and people can be tested while working or studying. 3. Non-contact detection can avoid the unwarranted influence of contact equipment or wires on heartbeat detection. There are two main categories of non-contact detection: using cameras or using radar. The principle of using a camera is to obtain the heart rate by comparing the displacement of the human thoracic cavity in different frames. However, this method is highly dependent on the resolution of the camera and relatively constant light and shadow environment. If the light and shadow condition of the setting change suddenly, the results obtained by this method will significantly deviate.

Compared to the video-based algorithm, radar signal detection is less dependent on the environment and it is also more helpful to preserve people's privacy. In the first research in last century, the microwave is the primary carrier of

heartbeat detection. Given that the chest displacement caused by heartbeat is in millimeters, the minimum wavelength provided by high-frequency microwave can achieve detection. From this century onward, most of the research in this field has focused on improving the accuracy of radar monitoring, reducing the weight and size of equipment, and expanding the detection range. Thus, hardware radar design, higher frequency, and fast, high precision software algorithm have been the focal points of such study. My research focuses on the algorithm level. Many algorithms have been tried based on the use of a more advanced frequency modulated continuous wave (FMCW) radar.

1.2 Motivation and Objectives

The motivations of the dissertation are as follows:

1) Artifacts generated by human body motion when detecting heartbeat can be removed by using the time sparsity gap between it and vital signs signals. Based on this idea, the SC-based algorithm is completed in [1]. This algorithm has poor adaptability to complex phase noise and the SC algorithm is not applicable under several conditions.. This thesis attempts to improve this shortcoming with CSC based on GMM improvement.

2) The use of separation algorithms to remove motion and breathing components in IF signals has been widely used. After separation, the source of each component is often simply proposed. We use a multi-feature-enhanced clustering method to cluster the separated components to obtain a purer heartbeat component.

1.3 Approach and Contribution

The accurate detection of vital signs including heartbeat rate and respiration rate using radar has important significance in many applications. In the first work of this thesis, an advanced algorithm based on convolutional sparse CSC and GMM is proposed for extracting the vital signs. In this study, vital signs are modelled by sparse coding and recovered by exploiting the sparsity of the signals in the frequency domain. GMM is introduced to model the unknown noises, which could be a mixture of multiple noise sources. The parameters of GMM , dictionary and codes, are updated by the expectation maximisation (EM) algorithm. To achieve faster processing, convolution computing is processed in the frequency domain. The method is tested by simulation and experiments. The results show that our proposed algorithm can accurately extract the vital signs.

In the second work of the thesis, an advanced version of singular spectrum analysis (SSA) is proposed for extracting heartbeat signals from the target with RBM. In this study, phase information on IF signals are decomposed to hundreds of components. An additional unique clustering step is adopted to replace the grouping step. A new feature is also proposed to enhance the performance of clustering. This method was tested by multi-target experiments. The results indicate that our proposed algorithm can accurately extract the heartbeat component.

1.4 Organisation of the Thesis

The thesis is organised as follows.

Chapter 3 presents the developed GMM-CSC scheme. To be specific, Section 2.3 reviews the system model. A detailed methodology of the proposed scheme is presented in Section 3.2. In Section 3.3, the detailed experimental settings and the performance results are provided.

Chapter 4 presents the Advanced SSA for extracting the heartbeat signal. To be specific, Section 4.2 reviews the system model. The detailed methodology of the proposed scheme is presented in Section 4.3. In Section 4.4, the detailed experimental settings and the performance results are demonstrated.

The conclusion and discussion are finally laid out in Chapter 5.

Chapter 2

Literature review

This chapter introduces the existing research methods of using FMCW radar to measure heartbeat; the advantages and disadvantages of each method are proposed in this chapter. At the same time, I will point out the uniqueness of my method at the end of this chapter. Picture 2.1 to 2.5 come from [37] and the resolution is limited.

2.1 CW Radar for Heartbeat Monitoring

In this section, a basic theory for heartbeat detection using CW radar is presented. Fig.2.2 is a schematic diagram of heartbeat measurement using a CW radar.

The emission signal model can be expressed as

$$T(t) = cos[2\pi ft + \Phi(t)] \tag{2.1}$$

where f is the frequency, and Φ is phase noise. If we use c as light speed the reflected signal captured by the receiver is:

$$R(t) \approx cos[2\pi ft - \frac{4\pi d_0}{\lambda} - \frac{4\pi x(t)}{\lambda} + \Phi(t - \frac{2d_0}{c})] \tag{2.2}$$

where d_0 is the distance between the radar and human body and $x(t)$ is the physiological movement. The phase of the received signal is modulated by the periodic motion caused by vital signs. If this local oscillator (LO) signal is used to down-convert the received signal, the baseband signal obtained will be determined by $x(t)$

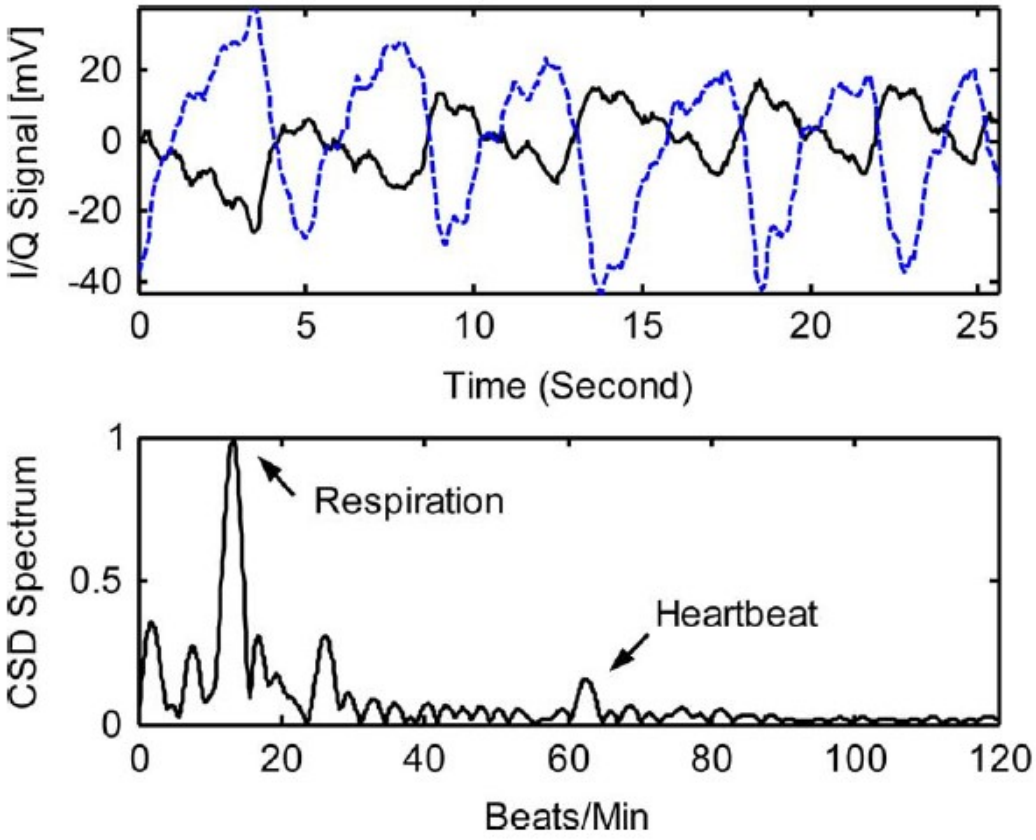

Figure 2.1 : I/Q output and vital signs detected

and d_0.

$$B(t) = cos[\theta + \frac{4\pi x(t)}{\lambda} + \Delta\Phi(t)] \tag{2.3}$$

where θ is determined by d_0 and $\Delta\Phi(t)$ is oscillator phase noise. After ADC, digitisation can be processed to identify information related to physiological movement. Fig.2.1 shows an example of using a CW Doppler radar to detect the baseband signal. Filtered signal in different domain is shown in different picture. The radar chip has two output channels (I/Q).

The system does not need a synchronization mechanism. The frequency offset in the baseband is partially compensated by the local oscillator using the same signal,

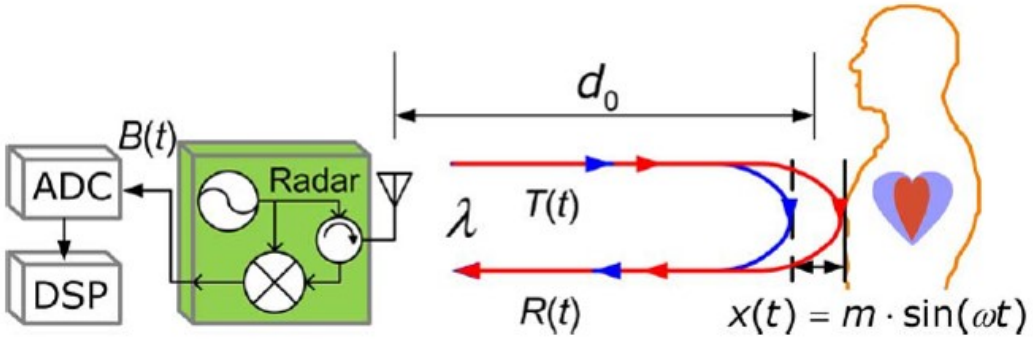

Figure 2.2 : Simple CW radar block diagram

so there is only a constant phase shift on the carrier. It should be noted that the radar block diagram in Fig. 2.2 is simplified. It is not enough to have the modules in the picture. Additional modules such as baseband amplifiers, down-conversion mixers and filters. In the knowledge of radar signals, if the phase noise of the two signals entering the mixer is uncorrelated, the phase noise of the local oscillator will mix with the received echo signal, destroying the required baseband signal. Within a short detection distance, the distance correlation effect significantly alleviates this problem. The use of the same transmit signal as the local oscillator of the down-converter can effectively eliminate the phase noise caused by the local oscillator. It is an ideal choice for high-sensitivity vital signs detection radars.

The selection of the carrier frequency is extremely significant. Carrier frequency determines the sensitivity and applicability of heartbeat measurement in different environments. Reference[2] has suggested that the optimal carrier frequency is also different for people with different physical intensity. Vital signs detection has been carried out for carrier frequencies ranging from hundreds of megahertz [3] to millimeter-wave [4] [5] [6]. In previous experiments, up to 228 GHz carrier was used for non-contact heartbeat detection. There are several advantages to using such

a high-frequency carrier signal. First, the frequency has at least 50 percent unidirectional transmittance in the atmospheric window. Second, a higher frequency can make the collimated beam maintain a more considerable distance to obtain a good aperture. The cross-section of vital signs may also increase with the increase of frequency. Finally, and most importantly, short-wavelength will increase the sensitivity of heartbeat detection. Considering that the heartbeat amplitude is so small, short wave measurement is of great significance. The cost of ultra-long-distance detection from the high-carrier frequency band (the maximum detection distance of the 228 GHz system is 50 M) is the lack of resolution. Breath and heartbeat will be difficult to distinguish. Too high a frequency causes the heartbeat to be completely covered by breath, and only when the subjects holds their breath can the heartbeat be measured.

When the amplitude of motion is significantly less than the wavelength, the baseband signal's mathematical expression can be simplified by linear approximation. If θ is an odd multiple of $\pi/2$, the baseband output is

$$B(t) \approx \frac{4\pi x(t)}{\lambda} + \Delta\Phi \tag{2.4}$$

If θ is an even multiple of $\pi/2$, the baseband output is

$$B(t) \approx 1 - [\frac{4\pi x(t)}{\lambda} + \Delta\Phi]^2 \tag{2.5}$$

Obviously, when theta is an odd multiple of lambda, the baseband output is proportional to the thoracic displacement, which means that we have completed the capturing this small displacement. When theta is an even multiple of lambda, the relationship between displacement and baseband changes, because the variable potion of theta mostly depends on the distance from the target, the null point will

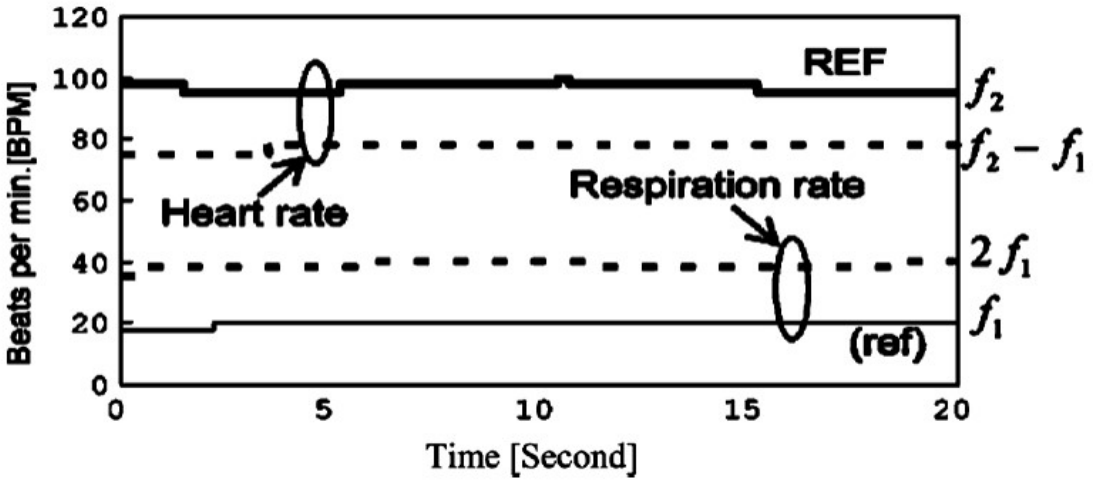

Figure 2.3 : Detection result at null observation point

appear at the same position as the distance to the radar target. The consequence of neglecting the null fact is severe, and measurement inaccuracy will occur frequently. Fig. 2.3 shows the detection result for the worst situation. In this situation, the measured "respiratory rate" is twice the actual value. The measured "heart rate" is the difference between the respiratory rate and the actual heart rate. [7] This kind of error will lead to frequent false positives and seriously affect the practical application. Using two receiver chains with a phase difference of 90 is an effective way to avoid detecting zeros. The two output channels of the quadrature receiver are as follows:

$$B_I(t) = cos(\theta + \frac{\pi}{4} + \frac{4\pi x(t)}{\lambda} + \Delta\Phi) \tag{2.6}$$

$$B_Q(t) = cos(\theta - \frac{\pi}{4} + \frac{4\pi x(t)}{\lambda} + \Delta\Phi) \tag{2.7}$$

For this chain receiver system, when one receiver channel is at null observation point, the other observation channel is at the optimum phase-demodulation point. This directly avoids the damage of observation zero to heartbeat detection. For this system, the worst situation is encountered when both $\theta + \pi/4$ and $\theta - \pi/4$ are odd

multiples of$\pi/4$. Neither chain is at the optimum observation point. At this time, the relationship between the motion amplitude and the baseband will become more complex. In most cases, the only option is to adopt the following formula to obtain the chest amplitude:

$$B_I(t) = B_Q(t) \approx \frac{1}{\sqrt{2}} - \frac{1}{\sqrt{2}[\frac{4\pi x(t)}{\lambda} + \Delta\Phi + (\frac{4\pi x(t)}{\lambda} + \Delta\Phi)^2]} \tag{2.8}$$

The above formulas holds when the wavelength is much larger than the amplitude of the chest cavity. At this time, the small-angle approximation simplifies our calculation and motion information can be obtained from the chain receiver through an adaptive algorithm, and there is no need to select the receiver manually. [8]

In recent work, the carrier frequency is mostly controlled at a 24 GHz - 80 GHz range to achieve measurement accuracy. At this time, the heartbeat amplitude is close to the carrier wavelength, and the small-angle approximation does not hold. A series of harmonics will be generated. If we use $x(t) = m * sin(\omega t)$ to define a simple periodic motion and decompose a complex movement into the sum of several simple motions, then the baseband signal can be expanded into

$$B(t) = 2 * \sum_{k=1}^{\infty} J_{2k}(\frac{4\pi m}{\lambda} * cos(2k\omega t) * cos(\Phi)) \tag{2.9}$$

$$-2 * \sum_{k=0}^{\infty} J_{2k+1}(\frac{4\pi m}{\lambda} * sin((2k+1)\omega t) * sin(\Phi)) \tag{2.10}$$

where Φ is the total residual phase and $J_n(x)$ is the nth-order Bessel function of the first kind [9]. The baseband signal after phase modulation is decomposed into many harmonics of the fundamental frequency. Although the motion frequency can be easily obtained from the carrier's fundamental frequency, the above formula also shows that the relative strength between harmonics depends on the residual phase

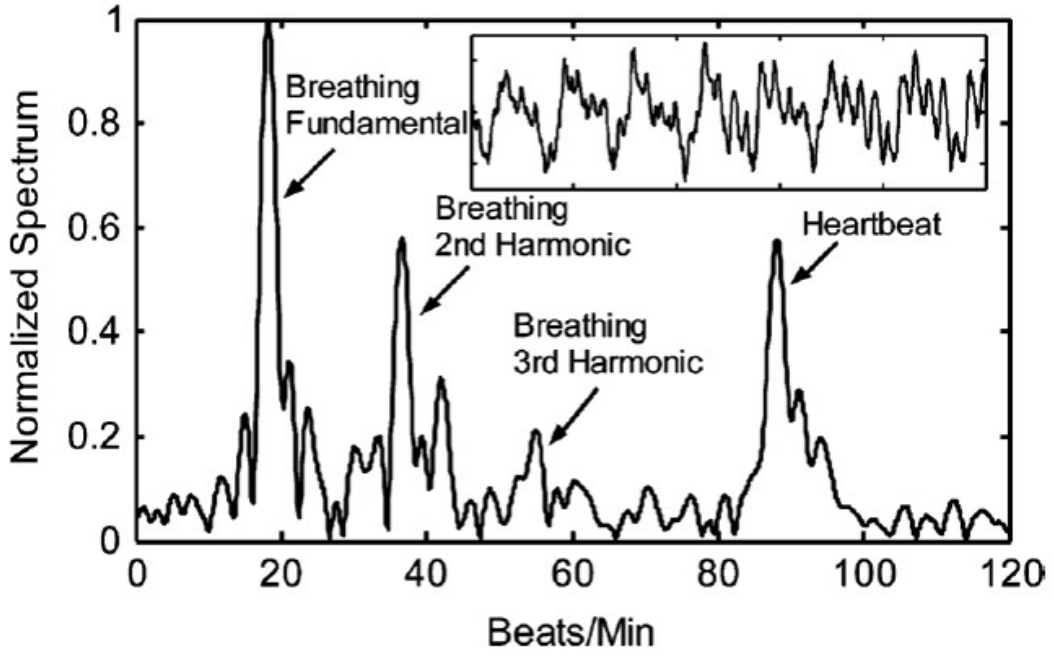

Figure 2.4 : Harmonics in normalized baseband spectrum

and motion amplitude for a specific carrier frequency. The relationship of harmonics is shown in Fig. 2.4. This relationship is based on experience.

An important challenge to heartbeat detection using CW radar is that phase noise can be converted into amplitude noise. Since the phase information is non-linear, it may interfere with the output strongly. When the same source is used for transmission and reception, the phase noise of the received signal is correlated with Lo's phase noise. For example, in the 50 cm range, the baseband noise at 10 Hz is signals 134 dB lower than the RF phase noise. The heart and respiratory information are encoded with 0.1 - 10 Hz phase modulation, and the phase noise is very complicated; so, distance correlation is significant in measuring chest wall motion. In Fig. 2.5, the predicted and measured phase fluctuation spectral density at delays of 6.2, 12.6, and 28.0 ns, and offset frequencies from 1 Hz to 1 kHz is plotted. On average, the measured value is within 5 dB of the expected value. The

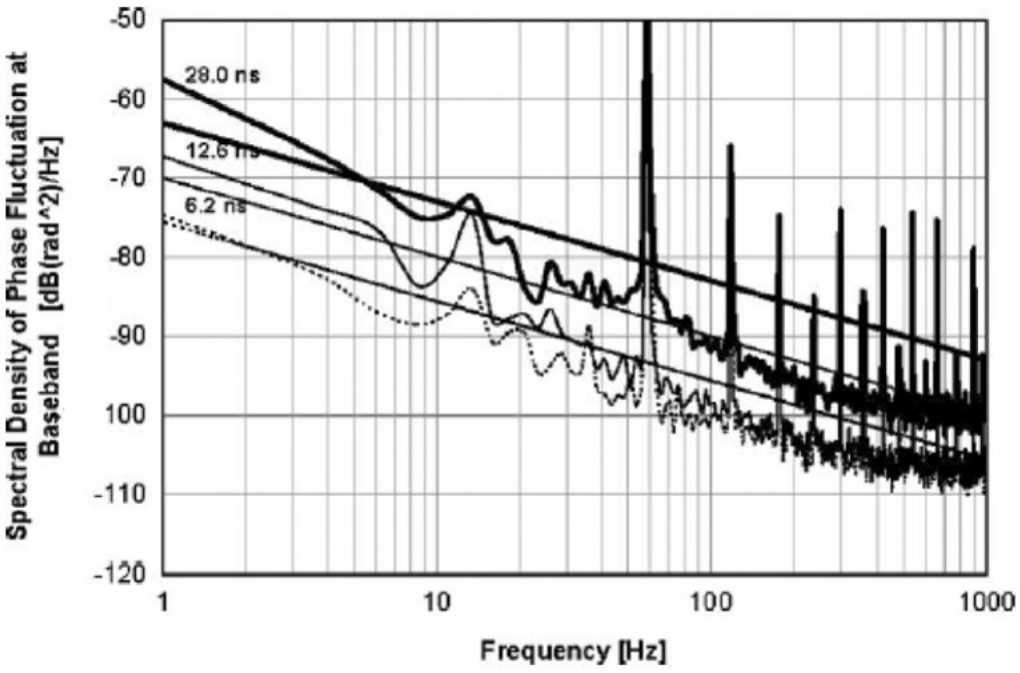

Figure 2.5 : Predicted and measured spectrum density of baseband phase fluctuation at baseband for different time delays

baseband phase noise is reduced from 148 DB to 136 dB at 1 Hz, and the time delay is reduced from 6.2 ns to 28.0 ns, corresponding to a 0.93 - 4.2 m range. The actual baseband noise spectral density is the same as the predicted range based on the range correlation theory [10] [11].

2.2 FMCW Radar for Heartbeat Monitoring

In this section, the original theory of using FMCW radar on detecting heartbeat is introduced. In FMCW theory, small angle approximation is not required. There is no limit to the relationship between the thoracic amplitude and wavelength.
Chirp is a sine wave or sine wave whose frequency increases linearly with time. Therefore, in this diagram of amplitude versus time, chirp can start from a sine wave with frequency f_c, gradually increase its frequency, and finally attain a frequency, such as FC plus B, where B is the bandwidth of chirp. Therefore, chirp

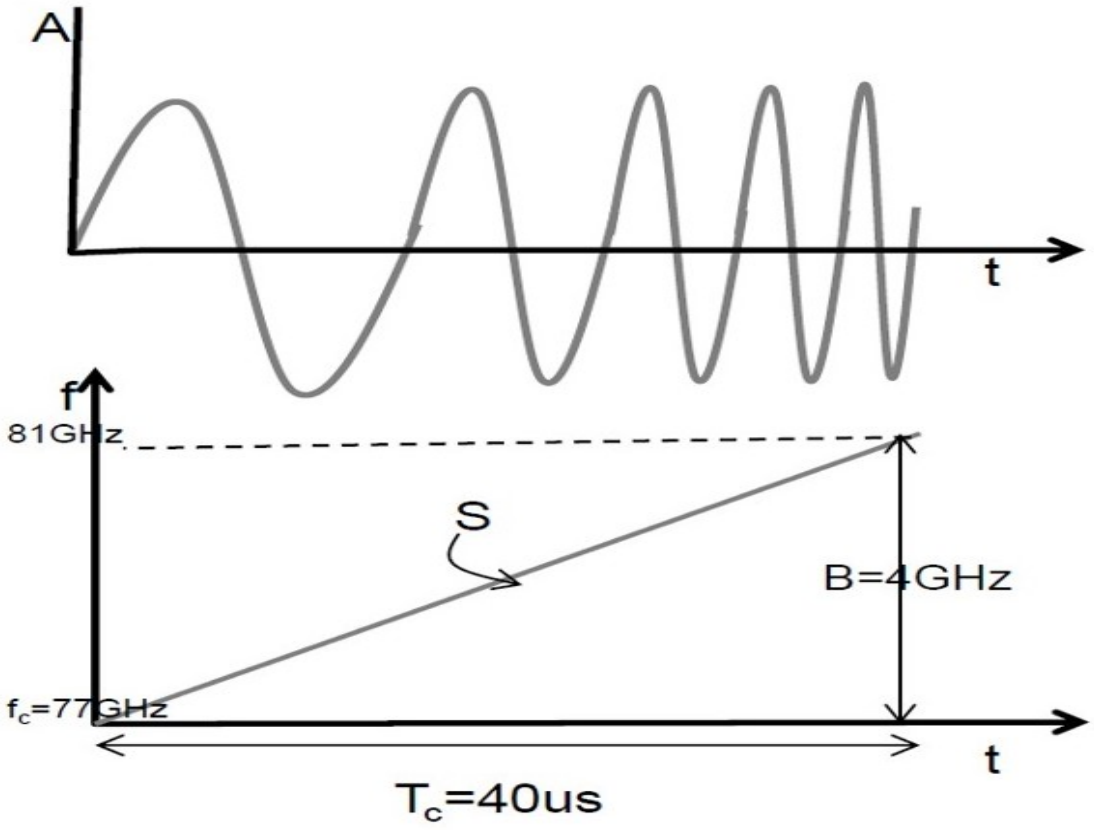

Figure 2.6 : T-A and T-F of chirps

is a continuous wave with linear frequency modulation. The time-frequency and time-amplitude relation of a single chirp can be presented in Fig. 2.6. Chirp signals can be presented as:

$$s_t = \sin(\omega_t t + \phi_t) \tag{2.11}$$

where ω_t represents frequency and ϕ is the initial phase. The frequency ω changes with time as $\omega_t = S * t + f_c, 0 \geq t \leq T_c$, where f_c is start frequency, S is the slope, and T_c is the duration. Fig. 2.7 is a simplified block diagram of an FMCW radar with a single transmitting antenna and a receiving antenna. Chirps are produced by synthesizer (①) and transmitted by transmitting antenna (②). The reflected chirp from the objective is received at the receiving antenna (③). The received and

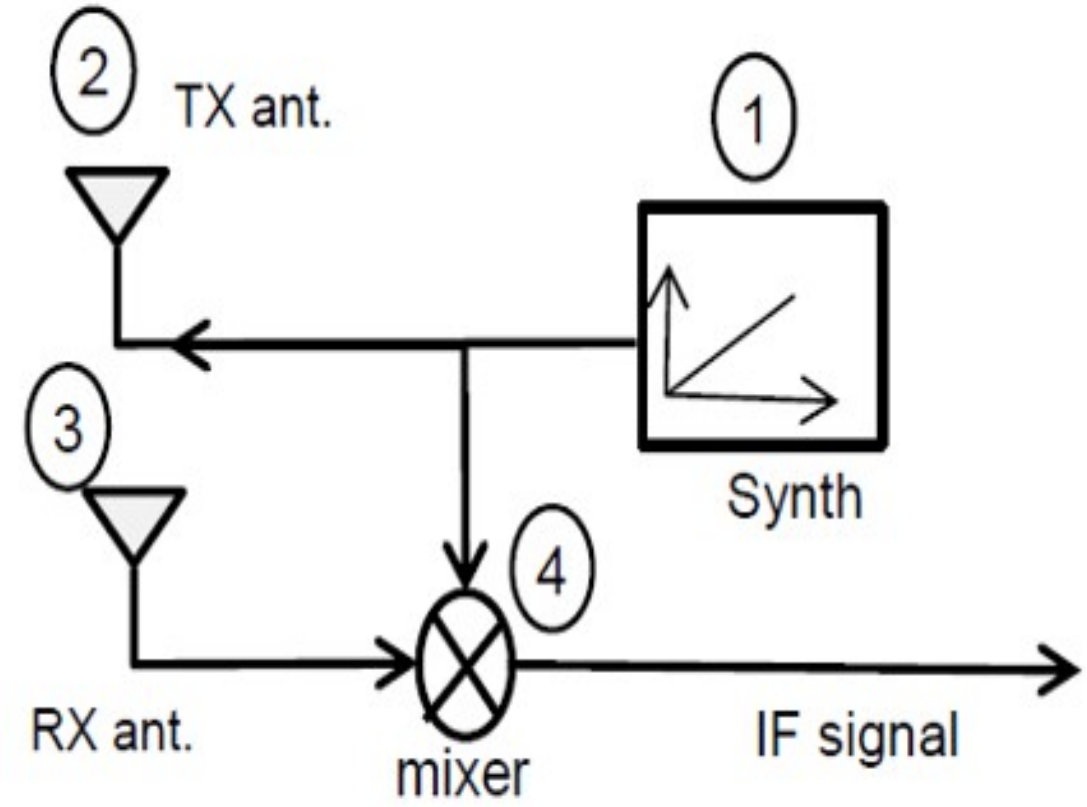

Figure 2.7 : Overview of FMCW structure

transmitted signals are mixed into intermediate frequency (IF) signal (④). The IF signal can be written as:

$$s_{IF} = \sin((\omega_t - \omega_r)t + \phi_t - \phi r). \tag{2.12}$$

If the object moves a small amount (for example, heartbeat movement) and round-trip delay $\delta\tau$. If signal will change accordingly. Fig. 2.8 will better describe the process (the new received signal after the blue curve represents distance change). The new IF signal's initial phase will be the phase difference at point D and the phase difference at point E as shown in Fig. 2.8. The phase of the RX chirp at E will remain the same as the original. However, the TX chirp phase at D will be the additional phase shift of the early phase $2\pi f_c \delta\tau = \frac{4\pi d}{\lambda}$, where d is the displacement

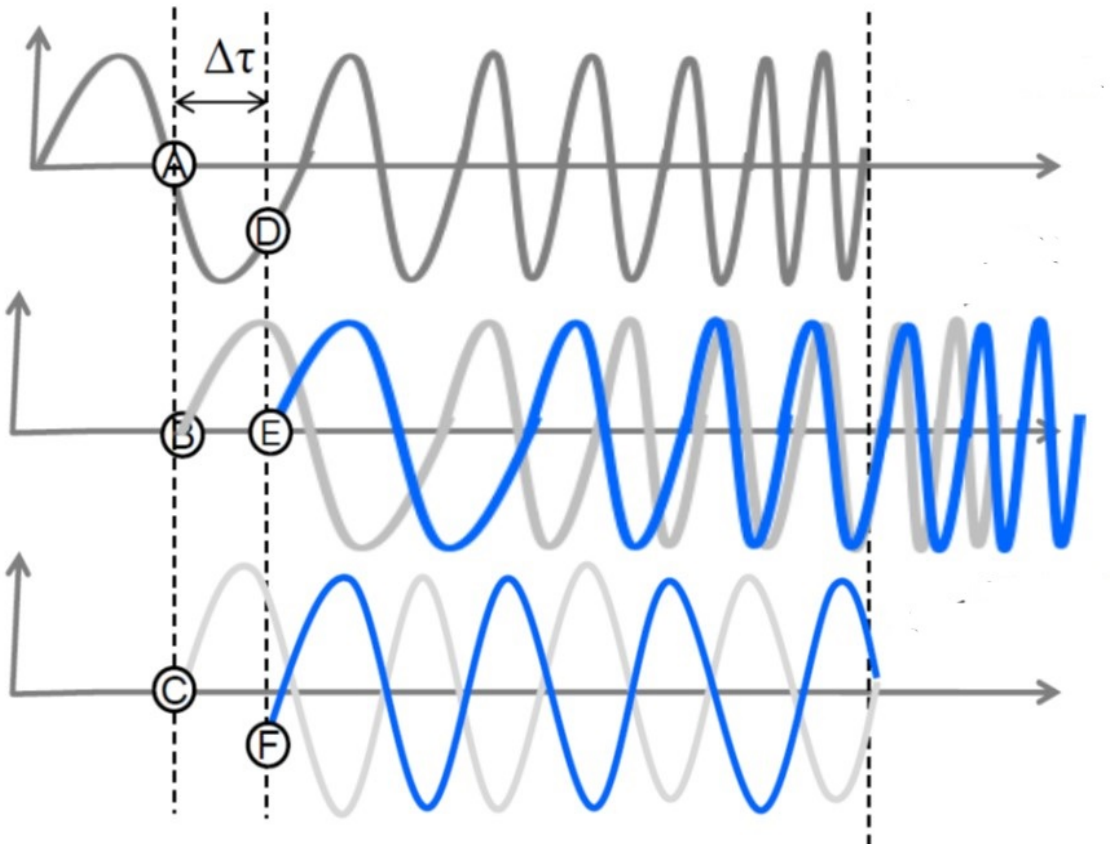

Figure 2.8 : IF signal change according to small distance change

change, τ is the arrival time delay caused by d, and λ is the wavelength. This means the phase difference between point a and point D is directly reflected in the phase of the IF signal.

In conclusion, chest vibration caused by vital signs may result in a slight change in the propagation path's length. Therefore, heartbeats can be determined by observing the peak phase in the frequency domain [12] [13].

2.3 RBM and RSM Cancellation

Since half a century ago, non-contact vital sign measurement has been widely studied. The micro-Doppler effect caused by small chest movements will be captured and reflected in the echo signal, as mentioned earlier. The millimeter waves emitted by the FMCW radar mentioned in this article can easily or more effectively penetrate

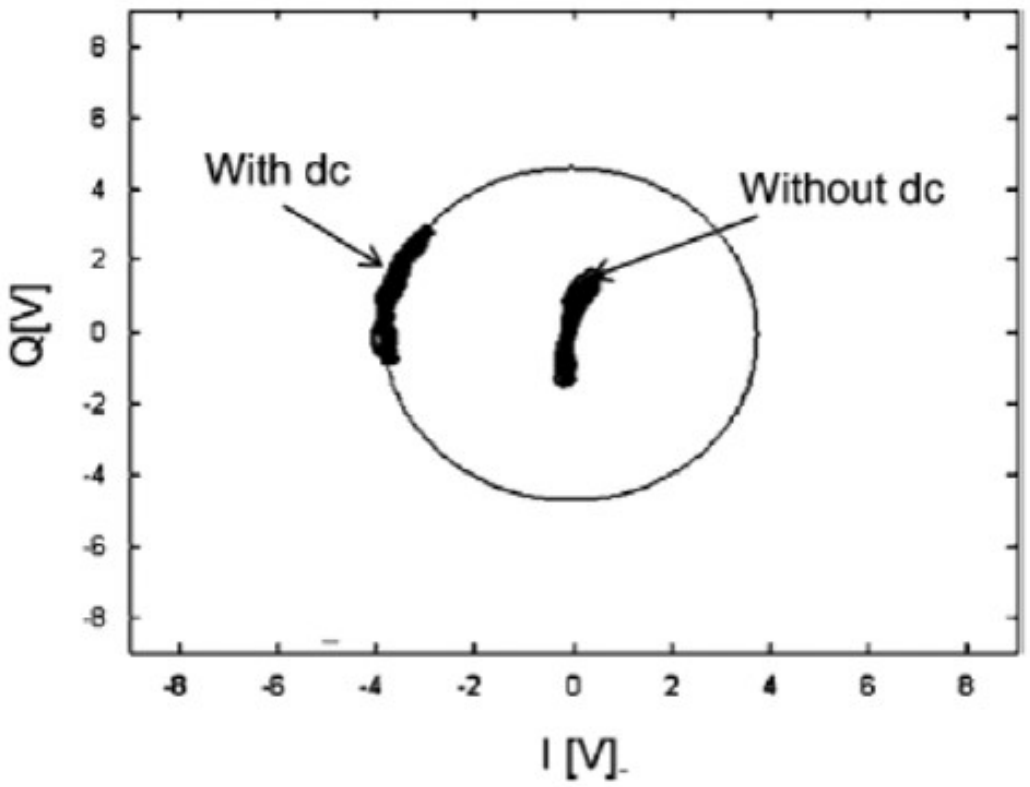

Figure 2.9 : Data constellation with or without DC information

objects and materials; so, the measurement method of shielding obstacles can also be realised. Many studies have overcome several obstacles in the past few decades and acheived breakthroughs, such as reciprocal tangential demodulation and miniature high-frequency radar chirps. Nevertheless, many challenging problems still persist in this area. The interference caused by these problems is often mixed with the chest displacement caused by the heartbeat; so, it is difficult to remove.

For heart rate detection using FMCW radar, the first problem is getting the correct phase for each chirp. The main methods to solve this problem are AT Decomposition, adaptive DC compensation [14] [15], and phase demodulation. This method can avoid the null observation point; phase information can be presented as $\Phi = arctan\frac{(Q(t))}{(I(t))}$. AT demodulation [7] is a scientific way to obtain phase. In

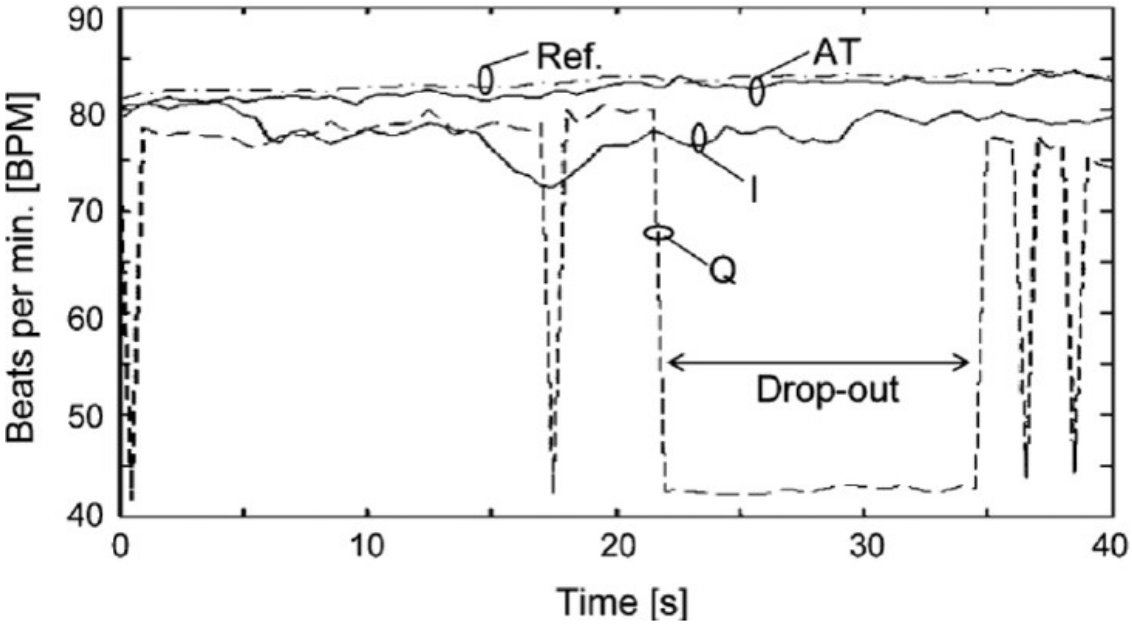

Figure 2.10 : The result measured at null point compared with wired finger pulse sensor

Chapter 2.1, it is observed that the Doppler phase shift caused by heartbeat is proportional to the motion shift of heartbeat to recover the required motion information reliably. Two significant issues affect the property of motion information recovery. First, the DC offset of the radar receiver is 0RF front-end output caused by circuit defects and the reflection of static objects (clutter) around the human. This will causes a demodulation error directly. Second, when the signal trajectory crosses the boundary of two adjacent quadrants, there will be a phase discontinuity in the function; so, an effective phase unwrapping algorithm must be used to recover the correct motion information. Therefore, to eliminate the discontinuity when crossing the boundary of quadrants in the spectrum, the AT demodulation algorithm is expressed as a multiple of 180, where the total undesirable DC offset is caused by clutter reflection. Fig. 2.9 shows a constellation of data with or without DC information. Fig. 2.10 shows the performance advantages of AT demodulated heart rate measurement. The signal demodulated by AT is measured at the position where the

channel is close to zero states. Through the detection from both sides of the human body, the random human motion noise is set to eliminate. When the SNR is too low, the digitisation process will be affected, and the channel rate will show the loss area, which is due to the square effect of vacancy. This proves that demodulation is very effective. DC compensation is often used alone for systems with less severe null observation. After several years of verification and improvement, these methods have become the first step for most phase information processing. Due to the non-linearity and limited precision, the noise caused by RBM and RSM remains in the data.

The second factor that interferes with heart rate monitoring is the periodic displacement of the chest caused by breathing. First, the displacement caused by respiration is greater than that of the heartbeat. The peak value of respiration and its co wave will cover up the heartbeat peak on the spectrum. Second, both heartbeat and respiration are sparse in the time domain. The algorithm using sparsity difference cannot remove the respiratory signal. The most popular method is to separate the respiratory component and the heartbeat component to remove the respiratory signal's influence on the heartbeat. For example, filters [16] and decomposition algorithms such as blind source separation algorithm (BSS) [17] are utilised. A problem with the usage of filters is that the breathing signal's harmonics are difficult to remove. Generally, the respiratory signal's third or fourth harmonics have a frequency and amplitude similar to the heartbeats. It is difficult to use filtering to completely remove the interference of breathing on heartbeat detection. The effect of decomposition is better than that of the filter. However, so far, neither of them can eliminate the impact of breathing on the heartbeat.

In addition to the interference of respiration on the heartbeat, another challenge

is the noise added to the signal by random body movement (RBM) and random system movement (RSM). It is very typical to use hardware upgrades and additional hardware to remove RBM. While measuring the chest cavity movement, the random movements of the person can be measured separately as compensation, and the RBM interference in the signal can be effectively removed. Fig. 2.11 shows an example of a hardware configuration. Two sets of transceivers are placed on the front and back of a person. Assuming that the person is lying flat on the bed and breathing, the two sets of antenna pairs are placed on both sides of the person's body. For the two groups of received signals, the vital signs signals are in phase, but RBM's part is just the opposite. This method is very useful, especially for subjects in a sleep state. Inadvertent turning over and limb swinging can be clearly distinguished and ignored, which reduces the vast majority of false alarms. A limitation of this method is that when the antenna pair is placed behind the person, the heart rate detection does not necessarily have a higher efficiency than the chest heart rate detection. Furthermore, human movement is sometimes complicated. It is not a simple swing back and forth swing or turning over. It is not comprehensive enough to consider human movement in a two-dimensional space. On this basis, [18] placed four sensors in four directions of the subject. Another similar method is to use two self injection locking (SIL) radars to detect heartbeat at multiple angles at the same time.

In many scenarios, multi-directional system settings are inconvenient. At this time, the system can only detect the heart rate from one side of the body. Fig. 2.13 shows a self-and mutually injection-locked (SIML) radar system capable of measuring heart rate. The system uses two different transmitting antennas to transmit signals to obtain an echo signal composed of two sets of doppler echoes with different weights. The RBM interference to the two receiving antennas can be adjusted to

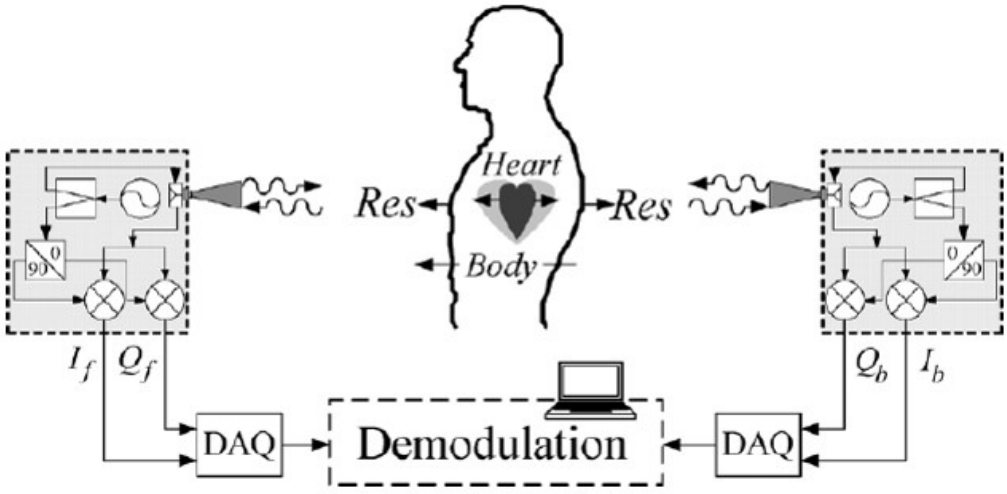

Figure 2.11 : The build of RBM noise elimination method based on the detection of both sides of the human body

the same magnitude by setting the antennas. Since the two SIL radars are out of phase and locked to each other, the RBM is naturally eliminated. Another way to eliminate RBM is to capture the human body's movement and compensate for RBM interference. This method is widely used in photoplethysmography (PPG) heart rate detection. In the radar system, because the system is far away from the person, it is difficult to directly obtain the person's motion information. Fig. 2.12 shows a method of capturing the human body's motion through a camera and compensating for the echo signal [19]. Considering the resolution and low-dimensional limitations of a single camera, the motion accuracy, and accuracy captured by this method are low. This also affects the accuracy of the camera-assisted algorithm. Furthermore, some studies have also used differential front-end Doppler radars operating at two different frequencies. Using dual antennas with appropriate beam widths, the human body can be illuminated at two adjacent positions for differential measurement. Since only one beam illuminates the heart, the baseband signal of the second radar can be used as a control to eliminate RBM noise.

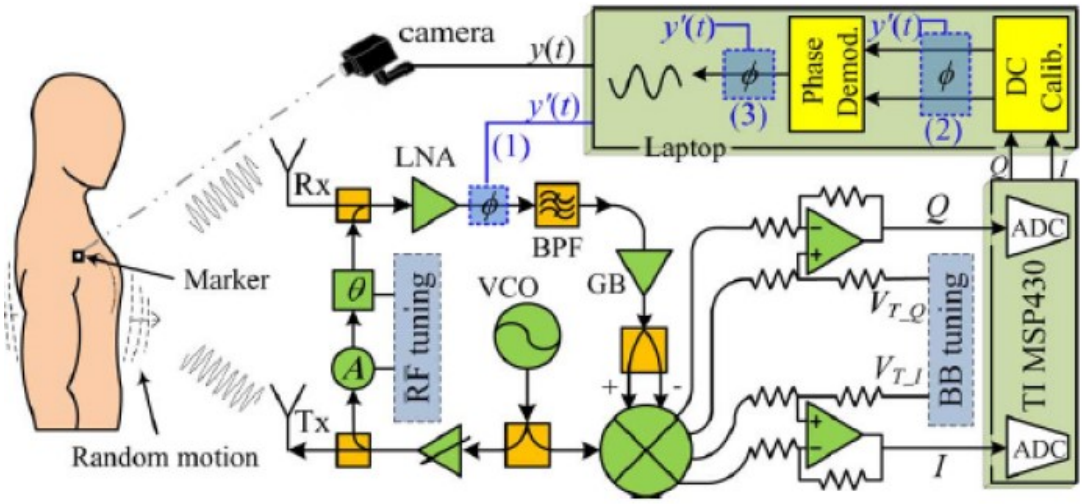

Figure 2.12 : The build of RBM noise elimination method based on a radar-camera sensing system

The use of software-based algorithms has become more popular in recent years. Software-based methods often require a simple pair of transceiver antennas, which greatly saves hardware costs and system space. The first problem faced when adopting such methods is the low signal-to-noise ratio of the echo signal. The low SNR data obtained from individuals with larger motion will hinder carrying out many algorithms. At present, the main method of pre-processing low SNR data is an adaptive matched filter, which is similar to improving the SNR of the GPS signal. Polynomial fitting is utilised in the data, which will produce a considerable error for the respiratory signal. For weaker motion, the primary problem is motion artifacts (MA). Most algorithms use the frequency domain to find the heart rate's peak value to determine heart rate. Artifacts will produce peaks at any position in the frequency domain and, sometimes, even hide the heart rate's peak value, which will greatly interfere with the algorithm's accuracy. In the past, many articles often asked subjects to lie on a bed or sit quietly on a chair [20] to avoid this problem. In both scenarios, the target's upper body is relatively static. For the scene of the subject's upper body movement, the target's motion information can be captured to

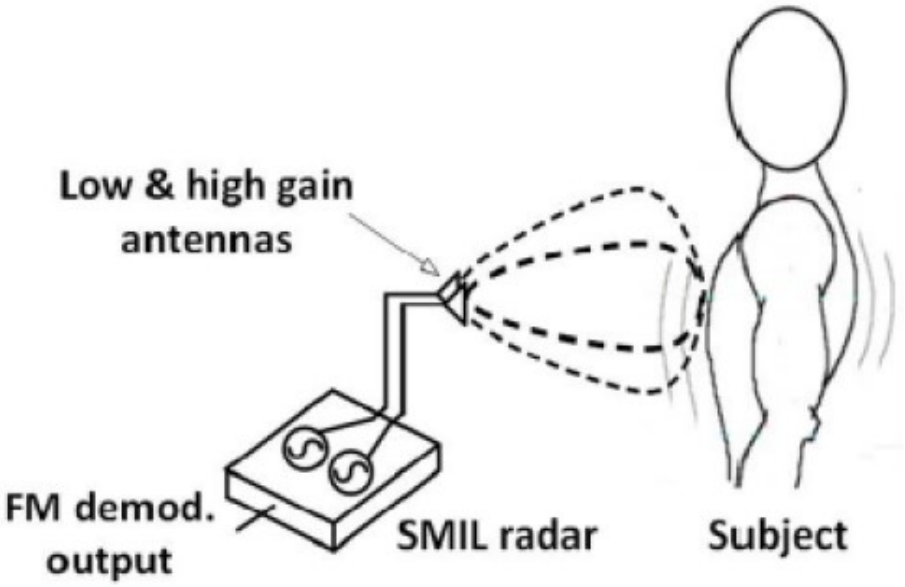

Figure 2.13 : The build of RBM noise elimination method based on a self- and mutually injection-locked radar architecture

compensate for the signal. This motion information is used to reference and remove similar components after decomposition. In [20], an additional transceiver antenna on the other side of the target is used to compensate for the signal, which is utilized to compensate for motion. Moreover, a camera and other methods are also used to capture motion and compensate signal, but the performance is not efficient. In general, additional equipment is required as assistance. Thus, the cost and practical inconvenience increase, and the scope of application is also limited. The core idea of remote processing methods is decomposition, i.e. dimensionality reduction. This implies that many traditional unsupervised learning dimensionality reduction methods can be useful. Many decomposition techniques have been proposed to remove MA like independent component analysis (ICA) [21], singular spectrum analysis (SSA) [22], Non-Negative Matrix Factorization (NMF) [17] and Empirical Mode Decomposition (EMD) [23]. ICA can not remove MA effectively because the statistical independence or uncorrelation of the different components ICA assumed is not

strictly established for MA and vital signs. Secondly, the multiple sensors needed by ICA do not meet the goal of reducing the size and weight of the device. As for NMF and other time-frequency domain methods, such as wavelet analysis [24], they have advantages of regional analysis that other single-domain analysis does not have. However, an issue emerges that pertains to accurately reconstruct the phase of the source. The error estimation of phase will lead to the upper limit of further reconstructed signal accuracy. As for EMD, it will decompose the signal into templates with a specific form as the mean value of the upper and lower envelopes is 0. EMD is extremely effective in simulation experiments because artifacts are artificially added. In reality, MA may appear in more complex forms; so, the performance of EMD will also be affected. Among them, SSA may be more effective. The main steps of SSA are embedding, decomposition, grouping, and reconstruction. The key to removing MA lies in the grouping step. [21] uses human hand movement information as an aid for grouping. Since wireless identification cannot obtain this auxiliary information, other features must be used to assist grouping. The eigenvalues of the time - frequency domain matrix are utilised in the group in [21].

In addition to the decomposition algorithm, some more common denoising methods, such as adaptive noise cancellation [25] [26], can be used. This algorithm depends heavily on selecting the reference signal; and sometimes, it isn't easy to reconstruct the qualified reference signal. This kind of method is different from the decomposition method as only vital signs are modeled. According to the characteristics of the heartbeat signal, the components that meet the conditions are extracted, and the rest of the components are regarded as noise, and this part is not focused. Algorithms that only focus on the target signal have worse performance in general. However, this is reasonable considering the small amplitude of the heartbeat compared to a more complex environment. In [1], CSC is used to process the signal, and

the time-domain sparsity difference between heartbeat and noise is used to extract heartbeat. CSC is introduced to detect heartbeat rates. The sparse characteristics of heartbeats in the time domain can be utilized to separate them from noise by sparse decomposition and rebuild algorithms. CSC has been widely utilised in image processing, motion recognition, trajectories analysis, and audio signal processing as an unsupervised machine learning algorithm. Unsupervised machine learning requires a few parameters so that this algorithm can be adaptive to environment variations. Compared to other algorithms, CSC works without requiring complicated parameter configuration.

The Gaussian model utilised by most algorithms for modeling noise can simplify the operation, but it is not consistent with the actual situation. In fact, the noise in the data can be regarded as a mixture of multi-source noise. In addition to the RBM mentioned above, the system's noise, the multipath, and complex environment also generate noises. In this case, my research uses the Gaussian mixture model to model the noise. This paper improves the CSC scheme by introducing the Gaussian Mixture Model (GMM) to model noises, including device noise and environmental interferences, in heartbeats detection. Due to the square loss function, conventional CSC algorithms generally utilize the Gaussian model to model noises, which may not reflect the real data noises. Noises in measurement signals can be caused by, e.g., movement of tiny animals, environments, the human body small movements, and the system itself, and its statistical distribution can be complicated [27]. Compared with existing methods, our GMM-CSC method uses fewer parameters, making training more straightforward while improving system performance.

Random system motion (RSM) is also one of the factors that interfere with heartbeat measurement. In most tasks, RSM is usually ignored. However, RSM

is also a challenge for high-precision heartbeat detection. In order to reduce the RSM interference, some work adopts the dual static radar, as shown in Fig. ref bistatic cite zhu2018fundamental for measurement. In the bistatic radar shown in the figure, the sensor node receives both the reflected signal from the human body and the direct signal from the transmitter. The interference of RSM to two echo signals should be similar. The similarity increases with the distance between the transmitter and the human body. In the case of long distance, the two kinds of noise will cancel each other after mixing. Another way to solve this problem is tracking. The idea is to isolate and track unwanted RSM by using signal processing methods such as adaptive noise cancellation (ANC) cite singh2013adative and separate it from radar output signal. Radio frequency (RF) cite rahman2015low tags have been used to track RSM. Figure ref RF shows an example of a label based approach. Under this condition, the reflected signal will only contain RSM information. The RSM information captured by this method can be used to compensate the received signal. Other methods include using SHSC. As shown in Fig. ref fhdf, FSC is transmitted to the object, while SHSC is transmitted to the fixed reflector. By using a high ratio antenna, the reflected SHSC contains only RSM related information. Therefore, the noise can be eliminated. In addition, similar to eliminating RBM, the random motion of the capture system can be used to compensate RSM.

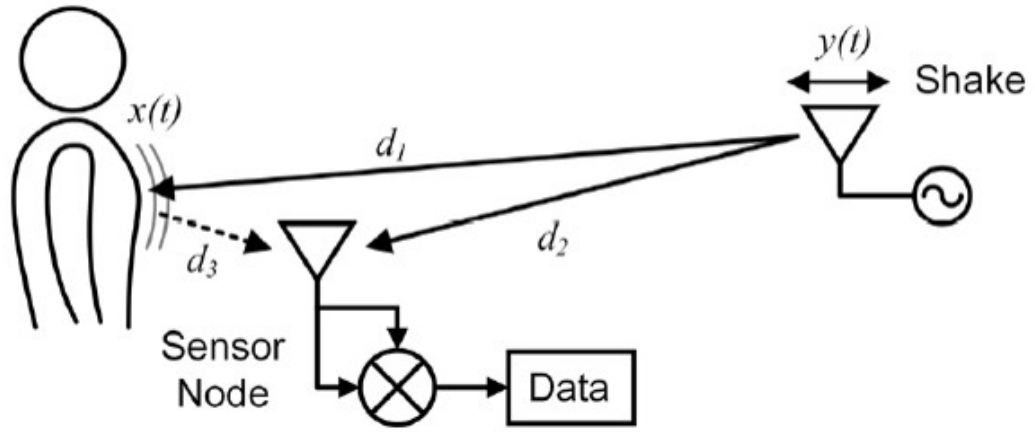

Figure 2.14 : The build of RSM noise elimination method based on a bi-static structure

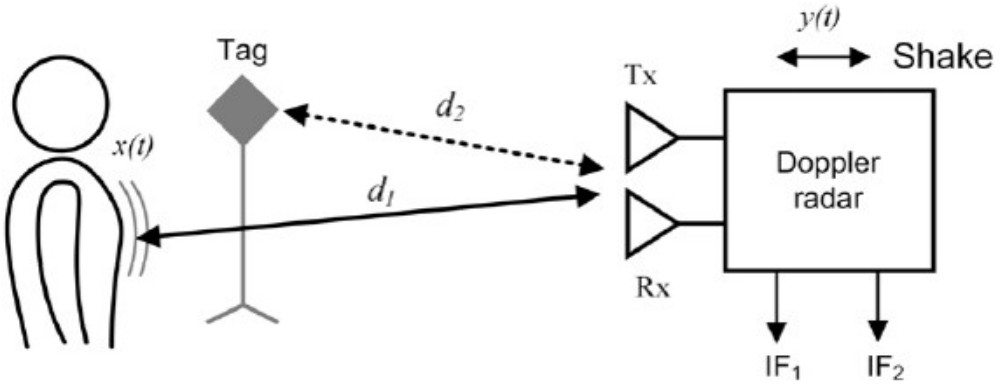

Figure 2.15 : The build of RSM noise elimination method based on a RF tag

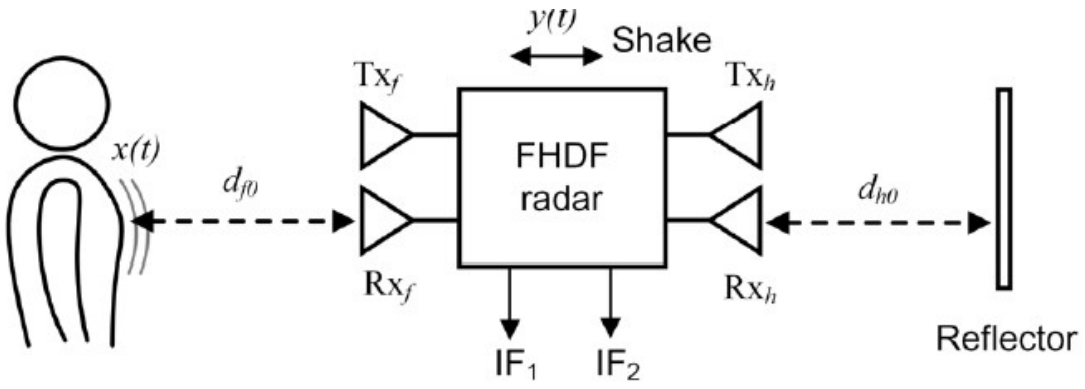

Figure 2.16 : The build of RSM noise elimination method based on a FHDF system

Chapter 3

Gaussian Mixture Model Based Convolutional Sparse Coding for Radar Heartbeat Detection

Complexed noise (including MA) removal is one of the most challenging tasks for radar-based heartbeat detection. To tackle this issue, in this chapter, we develop an advanced algorithm based on CSC and GMM for suppressing the interference and extracting clear heartbeat signals with an FMCW radar. The system model is firstly presented in Section 3.1. Section 3.2 deals with the methodology of the proposed scheme. To verify the performance of the proposed scheme, we conduct extensive experimental simulations in Section 3.3.

3.1 System Model

The structure of the system is shown in Fig. 3.1. It includes the following modules:

- Beat signal extraction: Extract the vibration information of the target;
- ADC: Convert raw continuous data to digital;
- Range FFT: Obtain the raw phase from the peak in every short-time matrix;
- DC compensation: Improve the quality of signals by compensating the DC component;
- Phase unwrapping: Unwrap phase for continuous displacement information; and

Figure 3.1 : System structure and signal pre-processing.

- GCSC: The module runs the GMM-CSC algorithm.

The operation of extracting the phase information from raw ADC data is elaborated as follows to Fig. 3.1. After sampling N points from the single chirp, the range-FFT is applied for a complex range profile. Repeating this for M chirps, a *range–slow time* matrix of size $M \times N$ is constructed. Each row of the matrix contains the information of the target at a given time. The position of the peak in each line represents the distance between the target and the radar, and the number of peaks corresponds to the number of objects. The small-displacement change, including heartbeats, is reflected in the phase of peak value. Before obtaining the angle of the complex data, it is necessary to ensure that any non-linearity, distortion, and artifacts have been eliminated. The phase calculation is highly non-linear, which increases the complexity of eliminating these defects. One method to improve phase quality is DC compensation. DC terms due to reasons rather than chest motions, for example the linkage TX to RX, will affect the accuracy of phase. Fig. 3.2 shows an example with an apparent shift before DC compensation, In this paper, columns in the $range - slow\ time$ matrix are presented in the I-Q axis. The DC component can be estimated by calculating the center of the point cloud data. After DC compensation the phases of each column in $range - slow\ time$ matrix is wrapped in $[-\pi, \pi]$. In contrast, the physical displacement may change beyond $\lambda/4$ (for a radar with frequency 60 to 64 GHz, $\lambda/4$ is 1.25 mm). Thus, the phase may change

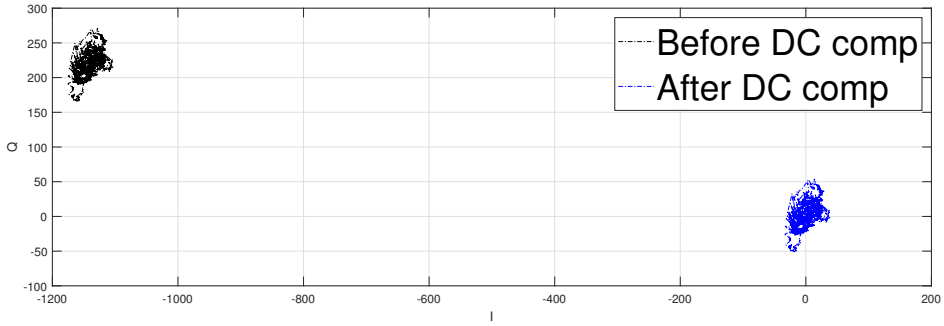

Figure 3.2 : Constellation correction of the received complex signal

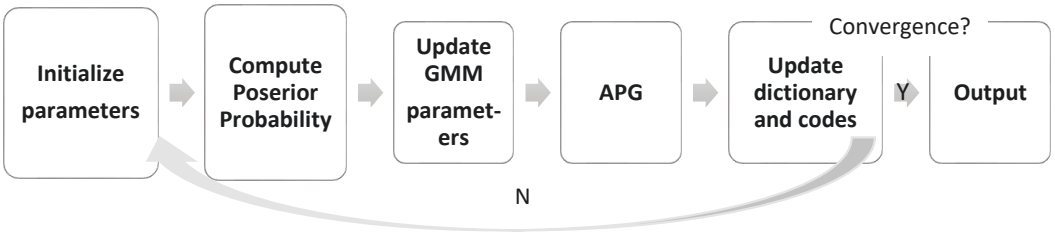

Figure 3.3 : Structure of GCSC

beyond $[-\pi, \pi]$. The detailed unwrapping operation is referred in [28]. After DC compensation and phase-unwrapping, the phase data is now ready for GMM-CSC. For better understanding, DC composition is normalization in I/Q domain.

3.2 Methods of GMM-CSC

This section presents the proposed GMM-CSC algorithm in detail, based on modeling the noises with GMM. In the first subsection, we use the expectation maximization (EM) algorithm for deriving the parameters of the GMM. In the second subsection, via adding a regular term, we translate the M-step into a traditional CSC problem. Following this we use a mature and accelerated optimization algorithm to solve this problem.

The main steps of the method are as follows, as represented in Fig. 3.3.

1. Initialize parameters;
2. Compute the posterior probability (the E-step);
3. Update the GMM parameters (one part of the M-step): update covariance matrix to maximize the expectation;
4. Accelerated Proximal Gradient (APG) (another part of M-step): Update the dictionary and codes by solving a CSC problem;
5. Go back to the second step, until the maximum iterations are reached;
6. Output the de-noised signal.

In the beginning of the algorithm, random initial values of the dictionary and GMM parameters (the number of Gaussian components G, covariance matrix Σ_g, and weight π_g) are given. The posterior probability of the mixture can be obtained by the Bayesian equation. In the M-step, we compute the derivative of the posterior probability to update the GMM parameters. A fast proximal gradient is used to update the dictionary and codes [29].

GMM and the EM Algorithm

If the dictionary has Dm elements the distance Y can be presented as:

$$Y_i = \sum_{k=1}^{Dm} d_k * z_{ik} + \varepsilon_i, \tag{3.1}$$

where i presents the ith sample and d_k and z_{ik} represent the element and corresponding codes, respectively. We can compute N samples at one time so $i \leq N$; ε_i is the combined noise caused by multiple factors as discussed before. Assume that noise N_i is a sample from a GMM distribution with probability density function

(pdf)

$$p(\varepsilon) \sim \sum_{g=1}^{G} \pi_g N(\varepsilon|0, \Sigma_g), \tag{3.2}$$

where G is the total number of Gaussian components.

The EM algorithm can be used to estimate the parameters that maximize the likelihood function of the GMM. I define a latent variable $\phi_{ik} \in 0, 1$, which indicates the assignment of the noise in the ith data to the kth Gaussian noise. From [30], log posterior probability is derived as:

$$E(\phi_{ig}) = \frac{\pi_g N(Y_i|\sum_{k=1}^{K} d_k * z_{ik}, \Sigma_g)}{\sum_{m=1}^{G} \pi_m N(Y_i|\sum d_k * z_{ik}, \Sigma_m)} = \gamma_{ig}. \tag{3.3}$$

Then the E-step is completed as

$$\begin{aligned} E(Y, \phi|\pi, D, z, \Sigma) = \sum_{i=1}^{N}\sum_{g=1}^{G} \gamma_{ig}(\log \pi_g - \frac{1}{2} log(|\Sigma_g|) \\ -\frac{1}{2}\frac{(Y_i - \sum_{k=1}^{K} d_k * z_{ik})^2}{\Sigma_g}). \end{aligned} \tag{3.4}$$

We can take derivation of (3.4) to maximum the upper bound:

$$\pi_g = \frac{1}{N}(\sum_{i=1}^{N} \gamma_{ig}); \tag{3.5}$$

$$\Sigma_g = \frac{\sum_{i=1}^{N} \gamma_{ig}(Y_i - \sum_{k=1}^{K} d_k * z_{ik})^\top (Y_i - \sum_{k=1}^{K} d_k * z_{ik})}{\sum_{i=1}^{N} \gamma_{ig}}. \tag{3.6}$$

From (3.5), we can update the sets π_g and Σ_g for every sample. After removing the updated parameter, the maximum of (3.4) is

$$\max \sum_{i=1}^{N}\sum_{g=1}^{G} \gamma_{ig}(-\frac{1}{2}\frac{(Y_i - \sum_{k=1}^{K} d_k * z_{ik})^2}{\Sigma_g}), \tag{3.7}$$

which is equal to an optimization problem

$$\min \sum_{i=1}^{N} \sum_{g=1}^{G} \gamma_{ig} (\omega_{gi} (Y_i - \sum_{k=1}^{K} d_k * z_{ik})^2), \tag{3.8}$$

where $\omega_{gi}(P) = \frac{\gamma_{ig}}{\sigma_g^2(P)}$. In order to ensure the sparsity of codes z, we can add a Lasso regularization part to (3.8) as

$$\min \sum_{i=1}^{N} \sum_{g=1}^{G} \gamma_{ig} (\omega_{gi} (Y_i - \sum_{k=1}^{K} d_k * z_{ik})^2) + \beta \|z_{ik}\|_1 \tag{3.9}$$

Separating the function into two parts, $F = f + r$ where $f = \frac{1}{2} \sum_{i=1}^{N} \sum_{g=1}^{G} \|w_{gi} \odot (Y_i - \sum d_k * z_{ik})\|_F^2$ and $r = \sum_{k=1}^{K} \beta \|z_{ik}\|_1 + I_D(d_k)$, with (w_{gi}) known F can be treated as a weighted CSC problem.

3.2.1 APG

Before using optimization methods to solve the above problems, this chapter explains the mathematical principles of APG and its variants. The global solution of non-convex problems is often difficult to obtain directly; so, extensive reseach is being carried out on solving non-convex problems by using APG. The optimization problem

$$F(x) = f(x) + g(x) \tag{3.10}$$

, where f is loss(smooth and convex) and g is convex regularizer, can be solved by the proximal gradient (PG).The convex regularizer can give a closed solution of the proximal step, which greatly simplifies the calculation process. In the face of non-convex problems in reality, such as the CSC problem faced in this work, the proximal steps are very difficult to analyse and calculate. The closed solution that is simple

and easy to solve can only be obtained from the convex regularizer. In 2015, the nonmonotone accelerated proximal gradient (nmAPG) algorithm was proposed to accelerate the optimization problem. nmAPG uses more than one proximal step to approximate complex proximal steps. This method greatly accelerates the descent speed, and there are special modules to ensure convergence in convex optimization. For non-convex problems, the convergence of nmAPG cannot be guaranteed.
In 3.10,f is L-Lipschitz smooth and g is proper, lower semi-continuous. If both f and g are convex, the $(k+1)th$ result is updated as

$$y_k = x_k + \theta_k(x_k - x_{k-1}) \tag{3.12}$$

$$x_{k+1} = prox_{\eta g}(y_k - \eta \nabla f(y_k)) \tag{3.13}$$

where θ is stepsize. The optimization process can be accelerated by controlling the θ. When we consider of non-convex problems, the convergence of the proximal gradient operator cannot be guaranteed. The nmAPG allows both F and G to be non-convex. To ensure convergence, additional proximal gradient operation is added. For future clarity, the algorithm of nmAPG is as Algorithm 1.

To make up for the shortcomings of nmAPG, a similar Nonconvex Inexact Proximal Gradient Algorithm (niAPG) was proposed.The algorithm of niAPG is as Algorithm 2.

The key to solving the non-convex optimization problem is ensuring that the target decreases sufficiently in each iteration. It always decreases sufficiently from x_k to x_{k+1}^p and extra checks are added to ensure decrease efficiency from x_k to x_{k+1}^a. If the decrease volume is not enough, x_{k+1}^p will replace x_{k+1}^a into the following calculations. In niAPG, the decreased efficiency mostly depends on the update of y_k. The check is placed after y_k's update. This prevents serious errors caused by bad extrapolation y_k. In order to speed up the entire optimization process, niAPG

Algorithm 1 The nmAPG Algorithm

input: $\eta \in (0, 1/L), positive\delta, \Delta_1 = F(x_1), q_1 = 1, andv \in (0, 1)$;
$x_0 = x_1 = x_1^a = 0 and t_0 = t_1 = 1$
for k=1,...,K **do**
$y_k = x_k + \frac{t^{k-1}}{t^k}(x_k^a - x_{k-1}) + \frac{t^{k-1}-1}{t^k}(x_k - x_{k-1})$
$x_{k+1}^a = prox_{\eta g}(y_k - \eta \nabla f(y_k))$
if $F(x_{k+1}^a) \leq \Delta_k - \frac{\delta}{2}\|x_{k+1}^a - y_k\|_2^2$ **then**
$x_{k+1} = x_{k+1}^a$
else$x_{k+1}^p = prox_{\eta g}(y_k - \eta \nabla f(y_k))$
if $F(x_k^a) \leq F(x_{k+1}^p)$ **then**
$x_{k+1} = x_{k+1}^a$
else$x_{k+1} = x_{k+1}^p$
end if
end if
$q_{k+1} = vq_k + 1$
$t_{k+1} = \frac{((4t_k^2+1)^{1/2}+1)}{2}$
$\Delta_{k+1} = \frac{1}{q_{k+1}(vq_k\Delta_k + F(x_{k+1}))}$
end for
Return x_{k+1}

Algorithm 2 The niAPG Algorithm

input: $\eta \in (0, 1/L), \delta in (0, \frac{1}{\eta} - L)$;
$x_0 = x_1 = 0$
for k=1,...,K **do**
$y_k = x_k + \frac{k-1}{k+2}(x_k - x_{k-1})$
$\Delta_k = max_{t=max(1,k-q),...,k} F(x_t)$
if $F(y_k) \leq \Delta_k$ **then**
$v_k = y_k$
else$v_k = x_k$
end if
$z_k = v_k - \eta \nabla f(v_k)$
$t_{k+1} = \frac{((4t_k^2+1)^{1/2}+1)}{2}$
$x_{k+1} = prox_{\eta g}(z_k)$
end for
Return x_{k+1}

has only one proximal process. Inaccuracies may be brought. The limit of decrease in each iteration is determined by q. If q is greater than 0, an occasional increase is allowed. When q is equal to 0, $F(y_k)$ is required to decrease strictly after every iteration.

Due to the unavoidable inexact problem, the niAPG algorithm must be proved to be convergent. Only an effective algorithm has the ability to converge. In the problem Fig. 3.2.1, if f is non-convex, and g is convex, then

$$s_{\eta g}(x) = \frac{1}{2}\|x - z_k\|_2^2 + \eta g(x) \tag{3.14}$$

be the objective in the proximal step. And the duality of the proximal at z_k is

$$max_{\omega} D_{\eta g}(\omega) = \eta(z_k^T - g^*(\omega)) - \frac{\eta^2}{2}\|\omega\|_2^2 \tag{3.15}$$

To ensure convergence, the upper bound of convergence $\epsilon_k = s_{\eta g}(x_{k+1}) - s_{\eta g}(prox_{\eta g}(z_k))$ must be less than a given value. When g is non-convex, the Gradient Decsent algorithm allows inaccurate proximal steps. However, it does not support accelerated and non-monotonic updates. Therefore, its proof of convergence cannot be used here. Since g is non-convex, it is challenging to derive the duality of the corresponding proximal step, and the optimal duality gap can also be non-zero. Therefore, we monitor the progress of F instead. This condition is also used in the Gradient Decsent algorithm. However, this requires checking an unrealistic additional condition:

$$F(x_{k+1}) \leq F(v_k) - \frac{\delta}{2}\|x_{k+1} - v_k\|_2^2 \tag{3.16}$$

CSC

We chose the accelerate proximal gradient (APG) method to solve the CSC problem. APG and its variances are one of the most effective methods for solving non-smooth optimization problems. Almost all APG algorithms can reach the convergence rate of $O(1/k)$. We can update d_k and z_{ik} by using APG. The APG algorithm is summarized in algorithm 3. Using the outputs from the algorithm we can update d_k and z_{ik}.

Algorithm 3 The niAPG Algorithm for CSC

input: D,z,J,λ,β,$t^0 = t^1 = 1$,η
  for j=1,...,J **do**
    u_k^j=$d_k^j + \frac{t^{k-1}-1}{t^k}(d_k^j - d_k^{j-1})$ for all k
    v_k^j=$d_k^j + \frac{t^{k-1}-1}{t^k}(z_k^j - z_k^{j-1})$for all k
    for i=1,2,... **do**
      $a^0 = \eta * b^{k-1}$
      d_k^{j+1}=$prox_{\eta I_D}(u_k^j - (a^j)^{-1}\frac{\partial f(d_k,z_{ik})}{\partial d_k})$
      z_k^{j+1}=$prox_{\beta\eta\|\|_1}(v_k^j - (a^j)^{-1}\frac{\partial f(d_k,z_{ik})}{\partial z_{ik}})$
      if $F(d_k^j, z_k^j) \geq F(d_k^{j-1}, z_k^{j-1})$ **then**
        $b^k = a^j$
      else$a^{j+1} = \eta^{-1} * a^j$
      end if
    end for
    d_k^{j+1}=$prox_{\eta I_D}(u_k^j - (a^j)^{-1}\frac{\partial f(d_k,z_{ik})}{\partial d_k})$
    z_k^{j+1}=$prox_{\beta\eta\|\|_1}(v_k^j - (a^j)^{-1}\frac{\partial f(d_k,z_{ik})}{\partial z_{ik}})$
    $t^{k+1} = \frac{1+\sqrt{1+4*t^k}}{2}$
  end for
  Return d_k^{j+1}, z_{ik}^{j+1}

3.3 Simulation and Experimental Results

In this section, we provide simulation and experimental results to validate the efficiency of the proposed GMM-CSC scheme. We first use artificially generated data to simulate heartbeats for testing. We then conduct experiments using practically collected data with an FMCW radar. In both simulation and experiments, only the

step length (for optimization) and the regularization parameter require adjustment. Our proposed GMM-CSC method is compared to the known normal CSC algorithm and the one with applying a low-pass filter. Vital signs is simulated as a sine wave of different frequencies.

3.3.1 Simulation

We first construct a clean signal, which is composed of a respiratory signal with a frequency of 0.5 and an amplitude of 1.5, and a heartbeat signal with a frequency of 1 and an amplitude of 0.2. We mixed five types of noise, as shown in Table I. In the simulation the number of elements is set as 12 and each element has a length of 30 points. There are 200 points in the signal; so, the length of codes used in CSC is 171. The step size of every iteration is fixed and the number of iterations are set to 50 time. These parameters are very reasonable. For example, the respiratory rate is 0.5. In fact, an adult breathe about once every two seconds.

The simulation results for different methods are shown in Fig. 3.4. Fig. 3.4a and Fig.3.4b show the original signal we create and the signal with added mixed noises. Fig. 3.4c - Fig. 3.4e show the results of applying three processing methods.

Fig. 3.4c shows the result of processing the signal with a low-pass filter. The high frequency component of noise is eliminated; however, the low frequency component that is close to the vital sign frequency is not removed. Fig. 3.4d and Fig. 3.4e are the signals obtained by using normal CSC and CSC with GMM. Our proposed GMM-CSC exhibits improved performance. Firstly, the frequency domain

Noise Composition	Distribution
Guassian	$\mathcal{N}(0, 0.1)$
Laplace	$1.5 * \mathcal{L}(0, 0.8)$
Gaussian	$\mathcal{N}(0, 0.3)$
Gaussian	$\mathcal{N}(0, 0.7)$
Gaussian	$\mathcal{N}(0, 1)$

Table 3.1 : Parameters of different distributions.

Methods	Deviation
Low-pass filter	22.3731
Normal CSC	12.6231
CSC with GMM	8.2225

Table 3.2 : Results of different methods.

spectrum obtained by the normal CSC always contains components that do not belong in the original signal 3.5. Secondly, as shown in Table II, the deviation of estimation for the normal CSC is about 50% more than that for GMM-CSC.

3.3.2 Experimental Results

In the experiments, a Texas Instrument (TI) mm-wave radar (IWR6843) operating from 60 to 64 GHz is employed, and the maximal wavelength (at the 60 GHz band) is 4.99 mm. The frame period is 40 ms, and there are 128 chirps per frame. The sampling rate is 256 times per chirp. The maximal detection range is 2.14 m, and the vibration frequency resolution is 0.0782 Hz. The vibration frequency of the chest for the heart rate is in the $[0.8, 2]$ Hz range. For a typical adult, the amplitude of a heartbeat is about 0.5 mm to 0.8 mm. Both frequencies and amplitudes of the heartbeat signal are within the acceptable range of the radar; thus, they can be effectively detected.

Fig. 4.3 presents the initial scene setting for the experiment. The distance between the subject and radar is 50 cm at the beginning and steps up by 10 cm each time until 100 cm. The length of the collected data each time is also an the important parameters. Though data collected over longer time can lead to higher frequency resolution, HR always changes with time. As such it is not suitable to select data with a period of 30 s or longer, as mentioned in [31]. Additional algorithms adaptive to the variations of HR need to be further developed to allow continuous tracking. Here, signal data of approximately 5 seconds is used each time.

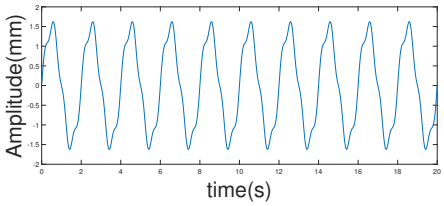

(a) Original simulated signal.

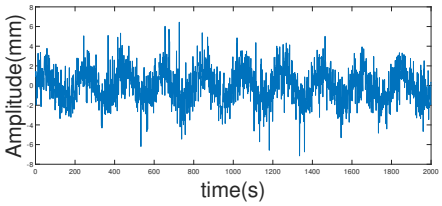

(b) Signal with mixed noises.

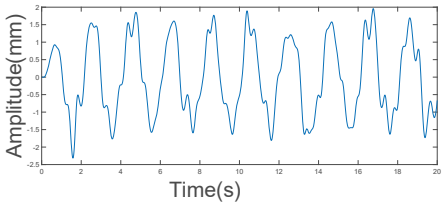

(c) Result of using low-pass filter.

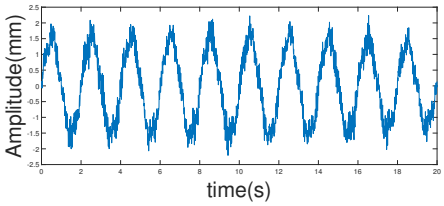

(d) Result of normal CSC algorithm.

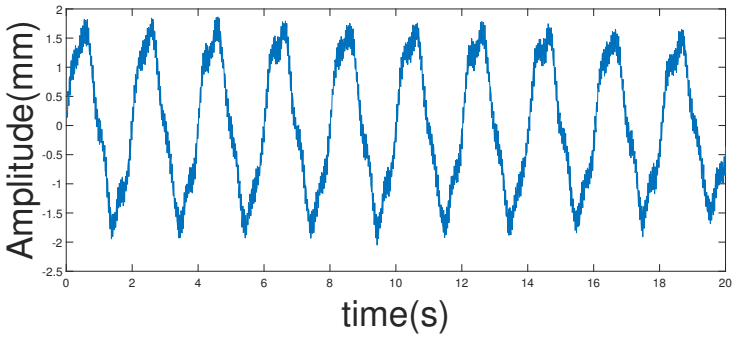

(e) Result of CSC algorithm with GMM.

Figure 3.4 : Simulation result

As shown in Fig 3.7, vibrations caused by heartbeats are obvious. It is not feasible to obtain the heart rate directly from the unprocessed data because respiratory harmonics and other noises interfere the heart rate in the frequency domain.

A band-filter with band pass $[0.4, 5]$ is utilized to remove respiration component. The frequency spectrum obtained before and after applying the GMM-CSC algorithm are shown in Fig. 3.8a and Fig. 3.8b. Only principal components are presented through adjusting the code sparsity and the main ingredient in frequency domain gather around one peak. The heartbeat spectrum is shown in Fig. 3.9. The HR is approximately 1.6 Hz. Taking the limited resolution and leakage effect,

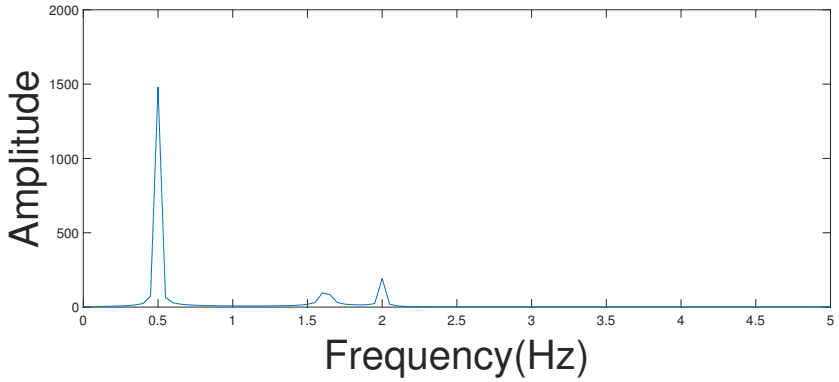

(a) Result of normal CSC in Frequency domain.

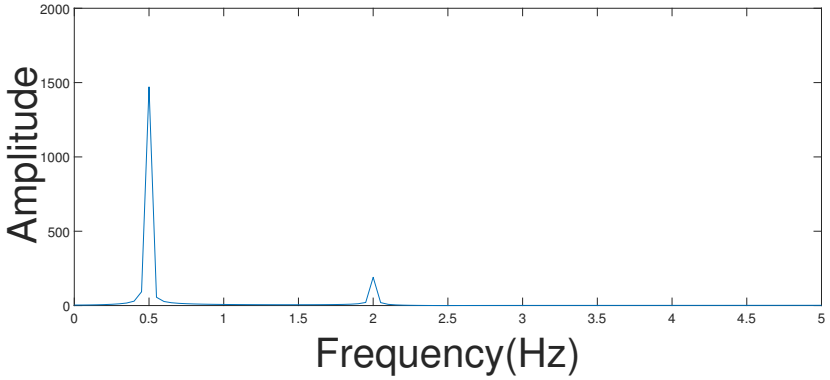

(b) Result of CSC with GMM in Frequency domain.

Figure 3.5 : CSC and GMM-CSC results in frequency domain.

the deviation is about ±0.2 Hz. Results compared to the other ones [28] [32] are presented in Table 3.3.

Experiments were also conducted on multiple targets . Fig 3.10 shows the scene of the two-target experiments. From the range-FFT figure (Fig. 3.11), two peaks can be separated easily. Phase information from two targets subsequently then be extracted from two separated peaks and the results are shown in Fig. 3.11. The figure indicates that vital signs for both people can be obtained. The distance between target 2 and the radar is larger; hence the heartbeat component extracted for target 2 is interfered. Targets with different distances will produce multiple peaks in the range FFT image, so they can be processed separately.

Figure 3.6 : Scene setup for experiment.

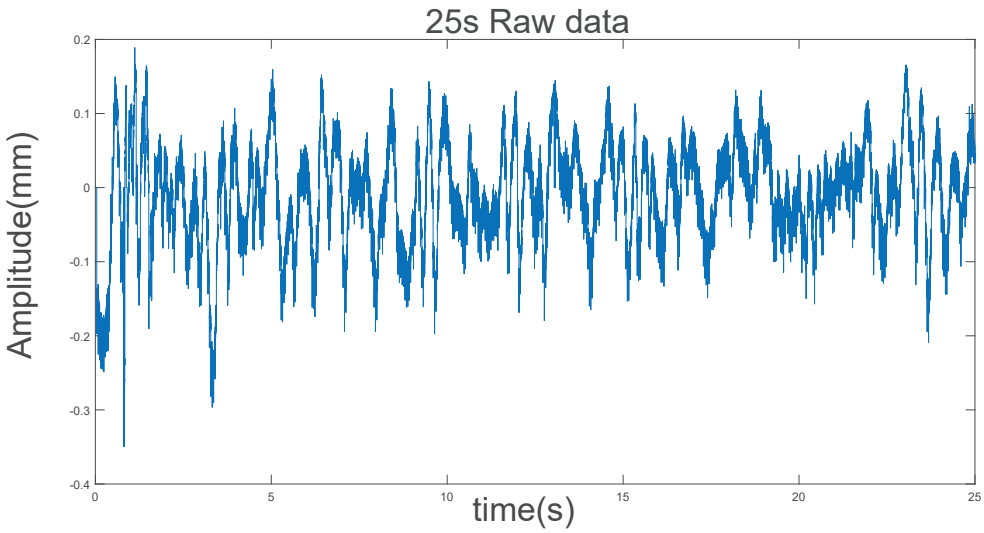

Figure 3.7 : Unwrapped-phase signal with time period 25 seconds

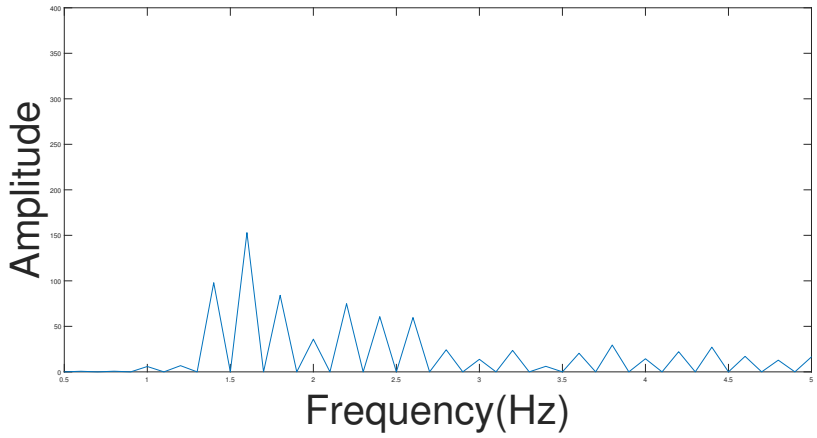

(a) Frequency domain spectrum before algorithm

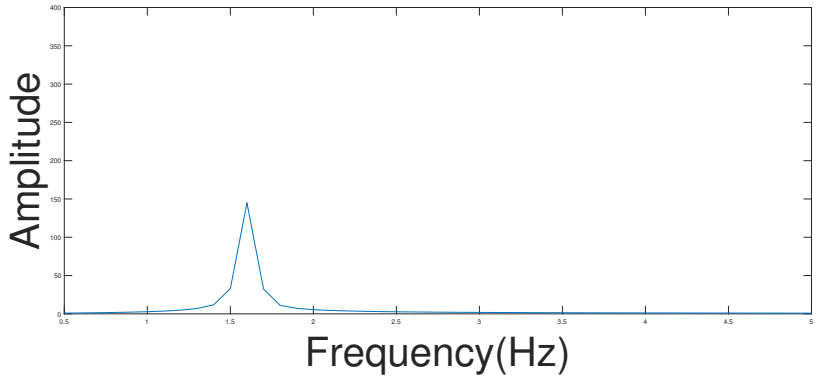

(b) Frequency domain after algorithm

Figure 3.8 : Change in frequency domain after GMM-CSC

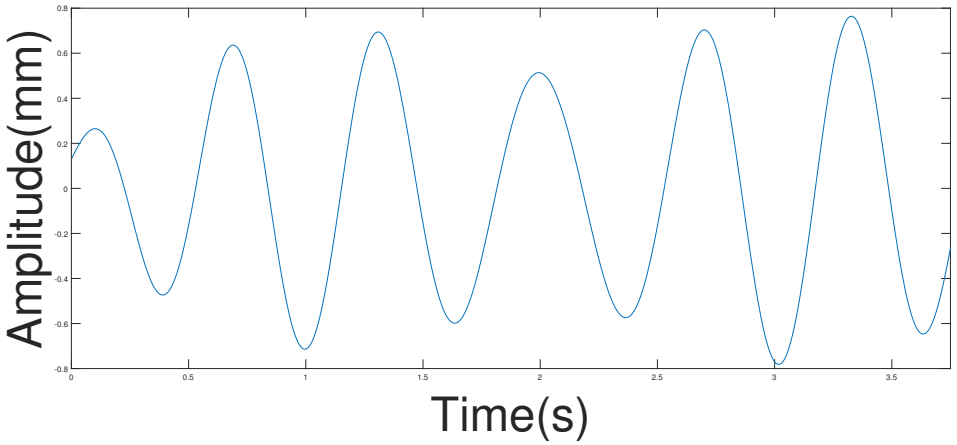

Figure 3.9 : Heartbeat signal extracted.

Ref.	Distance(m)	f_{min}(GHz)	Correct rate(HR)
[28]	1.7	77	0.80
[32]	1	80	0.87
Ours	1.6	60	about 0.88

Table 3.3 : Comparison with existing algorithms.

Figure 3.10 : Two-target experimental set up.

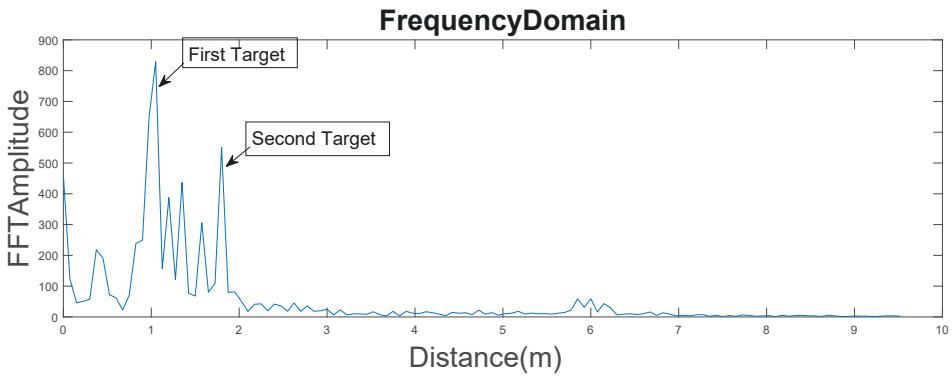

Figure 3.11 : Range-FFT figure.

Chapter 4

Advanced Singular Spectrum Analysis Method for Radar Heartbeat Detection

RBM removal is a challenging task for radar-based heartbeat detection. This chapter develops an advanced Singular Spectrum Analysis algorithm to remove the interference and extract clear heartbeat signals with an FMCW radar. The cluster methods and system model are initially presented in Sections 4.1 and 4.2. The methodology of the proposed scheme is presented in Section 4.3. Further, to verify the performance of the proposed scheme, we conduct REAL experiments in Section 4.4.

4.1 Cluster Methods

In this work, four cluster algorithms are utilized for comparison. They are K-means, mean-shift, EM, and Hierarchical. Both theory and features of the mentioned algorithm are introduced in this section.

K-means Cluster K-means is one of the most commonly used clustering methods. Although it has shortcomings, it is fast. K-means' time complexity is $O(tkn)$, where t is the iteration times, k is the number of clusters, and n is the amount of data. The specific steps of the algorithms are as follows:

1) First of all, we randomly initialize some of their centers. The center point is the position with the same length as each data point vector. This requires us to predict the number of classes (i.e., the number of centers) in advance.

2) The distance between each data point and the center point is calculated, and the nearest data point is classified into the same category.

3) The center point of each class is calculated as the new center point.

4) Repeat the above steps until the centers of each class change slightly after each iteration. The center point can be initialized randomly several times, and then the one that runs best can be selected.

The disadvantages of the algorithm are obvious. All cluster centers are random. In addition, the number of clusters, which is often difficult to judge, must be set in advance. Different cluster numbers will bring different results. This means that the performance of the algorithm may be volatile under a limited number of iterations.

Expectation Maximum Cluster with Gaussian Mixture Model K-means assumes that the data is spherical in space, while EM cluster assumes that the data is Gaussian mixture distribution, which offers more possibilities. Two parameters to describe the shape of the cluster: mean and standard deviation. Thus, these clusters can take ellipses of any shape because there are standard deviations in each direction. Therefore, each Gaussian distribution is assigned to a single cluster. The specific steps of the algorithm are as follows:

1) Select the number of clusters (similar to K-means) and initialize the Gaussian distribution parameters (mean and variance) of each cluster randomly. We can also observe the data and give a relatively accurate mean and variance.

2) Given each cluster's Gaussian distribution, calculate the probability that each data point belongs to each cluster. The closer a point is to the Gaussian distribution center, the more likely it is to belong to the cluster.

3) Based on these probabilities, we calculate the Gaussian distribution parameters to maximize the probability of the data points. We can use the weight of the probability of data points to calculate these new parameters. The weight is the probability that the data points belong to the cluster.

4) Repeat iterations 2 and 3 until there is little change in an iteration.

Since K-means can be considered a special EM algorithm, and EM often uses K-means as the initial value, the performance of EM is always better than that of K-means. Simultaneously, the EM cluster uses probability to express data attribution, and all data points can belong to multiple clusters. This is more conducive to correct clustering. However, similar to K-means, the EM cluster can easily fall into the optimal local value and cannot reach the optimal global value.

Mean-shift Cluster Mean-shift clustering is an algorithm based on the sliding window to find dense data points. This is a centroid based algorithm, which can locate the center point of each group/class by updating the center point's candidate points to the mean value of the points in the sliding window. Then, similar windows are removed from these candidate windows to form a central point set and corresponding groups. The steps are as follows:

1) Determine the radius r of the sliding window, and start sliding with the circle sliding window with radius r of the center point C randomly selected. Mean shift is similar to a mountain climbing algorithm, moving to the region with higher density in each iteration until it converges.

2) Every time you slide to a new area, calculate the mean value in the sliding window as the center point. The number of points in the sliding window is the density in the window. With each move, the window moves to the denser area.

3) Move the window, calculate the center point in the window and the density in the window, know that there is no direction to accommodate more points in the window. Thus, move until the density in the circle does not increase.

4) Sliding windows will be generated in steps 1 to 3. When multiple sliding windows overlap, the window containing the most points is reserved, and then clustering is performed according to the sliding window where the data points are located.

Mean shift clustering algorithm does not need us to know how many classes of data there are. Compared to other algorithms, the density based clustering algorithm is less affected by the mean. At the same time, the choice of window radius r may not be important.

Hierarchical Agglomerative Clustering Hierarchical clustering (HAC) is a bottom-up clustering algorithm. HAC first regards each data point as a single cluster, then calculates the distance between all clusters to merge the clusters until they are all aggregated into one single cluster. The steps involved in HAC are as follows:

1) Determine the radius r of the sliding window, and start sliding with the circle sliding window with radius r of the center point C randomly selected. Mean shift is similar to a mountain climbing algorithm, moving to the region with higher density in each iteration until it converges.

2) Every time you slide to a new area, calculate the mean value with the sliding window as the center point. The number of points in the sliding window is the density in the window. With each move, the window moves to the denser area.

3) Move the window, calculate the center point in the window and density, and know that there is no direction to accommodate more points in the window. That is, move until the density in the circle does not increase.

4) Sliding windows will be generated in steps 1 to 3. When multiple sliding windows overlap, the window containing the most points is reserved, and then clustering is performed depending on the sliding window where the data points are located.

The above three algorithms' output returns a plane unstructured clustering set; so, it is called flat clustering. One drawback of plane clustering is selecting the number of clusters and initial points, which is challenging work for inexperienced personnel because the quality of the clustering results depends on the selection of this parameter. This method avoids this shortcoming and is not sensitive to the selection of the distance metric. Therefore, the output of this method is stable. The only disadvantage is that the efficiency of this method is relatively low.
In general, clustering algorithms have their advantages and disadvantages, and clustering results vary greatly in different environments. This paper uses the above four algorithms to test and evaluate the clustering results of various clustering algorithms.

4.2 Pre-Processing and System Structure

The structure of the system is shown in Fig. 4.1. It includes the following modules:

- Beat signal extraction: Extract the vibration information of the target
- Range FFT: Obtain the raw phase from the peak in every short-time matrix
- DC compensation: Improve the quality of signals by compensating the DC component

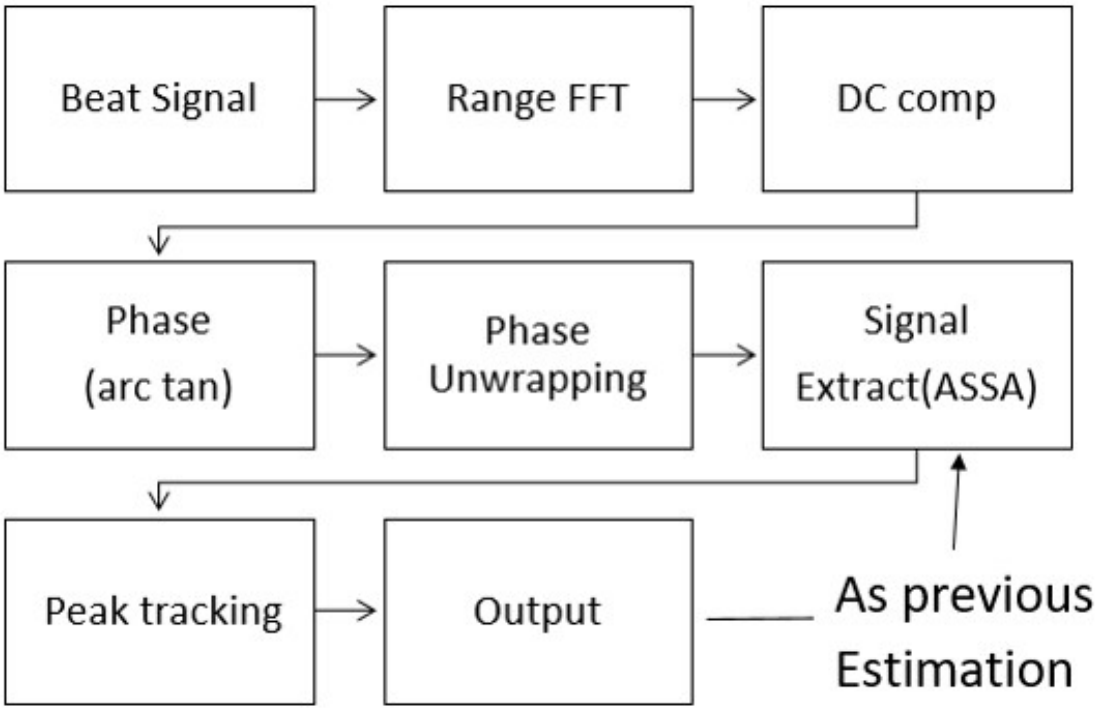

Figure 4.1 : System structure and signal pre-processing.

- Phase Extraction: Extract peak information from range FFT spectrum
- Phase unwrapping: Unwrap phase for continuous displacement information
- Advanced SSA: Extract heartbeat from noises
- Peak tracking: Track possible peak from heatbeat
- Output: Output the result for this time period and put it in the next window as previous estimation

In our frame, the pre-processing component is the general step of heartbeat detection using an FMCW radar. DC compensation helps to reduce errors, and phase unwrapping is utilized to obtain a continuous phase. After pre-processing, the phase signal (i.e. the displacement information) forms a sequence in the time domain. The target individual is asked to remain static for 3 to 4 seconds to utilize

the initial parts of the time series for accurate heart rate detection. After that, the time window moves forward. The size of the time window is set as 8 seconds, and every time it moves 2S. The result of this movement is that the heart rates in the two time windows will be very close. Therefore, each prediction result can be used as the next reference.

4.3 Advanced SSA for Heartbeat Extraction

This section presents the proposed advanced SSA algorithm in detail. First, we construct the matrix and perform SVD. Following this, we proposed a shape parameter to help the clustering operation.. The clustering method used and the following peak tracking are then discussed.

4.3.1 Signal Decomposition

Signal decomposition is one of the essential methods for extracting heartbeat. For example, independent component analysis (ICA) [33] is similar to the EMD and CWT mentioned above [21]. In these methods, the signal is divided into multiple parts, and the noise-related parts are removed. Thus, the remaining signal is interference-free. The existing problem is that without other prior information, it is difficult to identify the components generated by random motion. Our scheme seeks to determine the parts belonging to the heartbeat instead of linking them to the noise caused by motion. This ultimately provides two advantages. Firstly, for a target that is moving randomly, the heartbeat has very few components. After decomposition, only 2 to 3 components belong to the heartbeat. Secondly, compared to random human movement, the human heartbeat is more regular, and some prior information, such as trends, rate of change, and range, can be exploited.

The SSA method we use decomposes the sequence after pre-processing into oscillatory components and noise. A conventional SSA includes four steps: Embedding,

SVD, Grouping, and Reconstruction. In our proposed algorithm, the involved steps are Embedding, SVD, Reconstruction, and Clustering.

In the Embedding step, a time series $y = [y_1, y_2, y_3, ..., y_M]^T$ is mapped into an $L \times K$ matrix ($K = M - L + 1, L < M/2$) called L-trajectory matrix.

$$A = \begin{bmatrix} y_1 & y_2 & \cdots & y_K \\ y_2 & y_3 & \cdots & y_{K+1} \\ \vdots & \vdots & \ddots & \vdots \\ y_L & y_{L+1} & \cdots & y_M \end{bmatrix}$$

In the Decomposition step, the matrix A is decomposed by SVD as follows:

$$Y = \sum_{i=1}^{d} Y_i \qquad , d = \min(L, K), \tag{4.1}$$

where $Y_i = \sigma_i u_i v_i^T$ and σ, u, v represent the singular value, corresponding left and right singular vectors respectively.

4.3.2 Reconstruction and Clustering

After decomposition, the components corresponding to the larger eigenvalues will be reconstructed into the sequence y_p. The length of each sequence is M, corresponding to a component in y. The traditional grouping step will undertake simple grouping and stack the components with similar characteristics into one group before reconstruction. The feature is always the frequency or eigenvalue size. In [34], it supposes that the components y_p corresponding to the fourth-order of magnitude eigenvalues comes from the heartbeat. Considering that the third harmonic of respiration is very close to the heartbeat, this method may lead to mistakes.

The cyclostationarity of vital signs has been proposed as an useful parameter for

separating heartbeat from other components [35]. In fact, the cyclostationarity of the heartbeat signal is much stronger than that of other components, such as RBM or other noises. The common cyclostationarity detection methods need to manually determine the shape of the sequence's autocorrelation function or add the sequence into the detection function. These two methods are not feasible for heartbeat detection because a fast and quantitative method is required to determine the degree of a time series with cyclostationarity. The shape of the sequence's autocorrelation function is one of the effective parameters that can be used to evaluate this property. The curve of the autocorrelation function of an ideal cyclostationary sequence fluctuates in a small range around 0, while the one of an irregular fluctuation curve fluctuates immensely. By determining the discrete degree of the autocorrelation function's envelope curve, the cyclostationarity of the original sequence can be quantitatively evaluated.

In the clustering step, all y_ps are assigned into the cluster c. The set of d indices could be partitioned into c clusters $I_1, I_2, \ldots, I_c$. Thus Y can be decomposed as

$$y = \sum_{p=1}^{c} y_{I_p}, \quad y_{I_p} = \sum_{a \in I_p} y_p. \tag{4.2}$$

In this paper, we use two parameters to cluster the data. The first is the dominant frequency of the component: the reasonable frequency of heartbeat is between 0.6 and 2, which can be used as one of the basis for clustering. The second is the shape parameter of the component. The shape parameters S can be written as

$$S = L * \frac{Sd(E(\gamma_a))}{Mean(E(\gamma_a))} \quad , \tag{4.3}$$

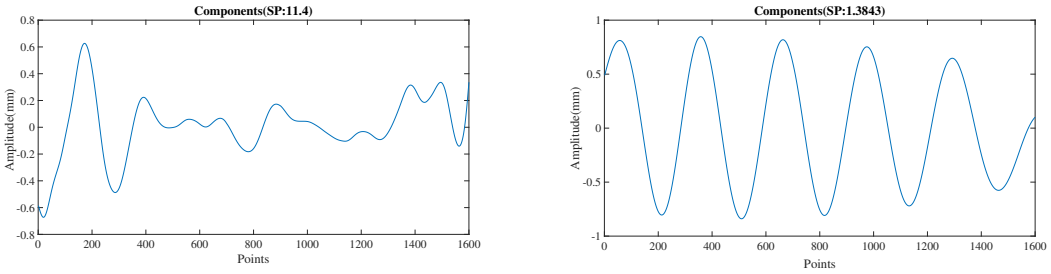

(a) Time series with large S (b) Time series with small S

Figure 4.2 : Comparison between two components with different S

or

$$S = L * c_v(E(\gamma_a)) \tag{4.4}$$

where γ_a is the autocorrelation function of y_p, $E()\dot{}$ is the envelop function, c_v is the coefficient of variation, L is the enlarge parameter, and Sd represents for the standard difference. Both sequences in Fig. 4.2 are decomposed components of the actual experimental data. Among them, the sequence with a smaller S-value obviously has more characteristics that heartbeat components should have: relatively stable period, and amplitude and no obvious monotony.

Clustering will be performed in a two-dimensional feature space, and all components become scattered points in the two-dimensional space.

4.3.3 HR Estimation

An effective traditional method of extracting heart rate is peak tracking. This method looks for possible heartbeat peaks near the heart rate estimation in the previous time window on the spectrum. This kind of peak tracking has two types of auxiliary information to verify whether it is correct, one is the harmonic of the heartbeat vibration, and the other is the peak value. If both are within a reasonable range, the peak value is regarded as the correct heartbeat estimate. If the two are

unreasonable, the previous estimate or average value is used to modify the estimate.

In this paper, a different method is utilized to estimate the heartbeat frequency. In the two-dimensional space after clustering in the previous step, the first step is to find the cluster center that is closest to the last estimation result and assume that this is the estimation in the current time window. Second, the time-domain signal is built by adding components corresponding to the chosen cluster. Subsequently, the time domain result is transformed into the frequency domain by FFT. The closest peak N with the last estimation is selected for the current period. We also use two other parameters (estimated result peak amplitude and estimated heart rate) to correct this result.

Let HR_c be the current estimation, HR_p be the last HR estimation, A_c be the current peak amplitude, and A_p be the last peak amplitude. Let us consider the following four cases.

$Case1$: If HR_c belongs to $(HR_p - 0.2, HR_p + 0.2)$ and A_c belongs to $(0.3 * A_p, 3 * A_p)$, then the selected peak N is the result for the current time window;

$Case2$: If HR_c belongs to $(HR_p - 0.2, HR_p + 0.2)$ and A_c is not in the range of $(0.3 * A_p, 3 * A_p)$, then the second closest peak N is chosen and re-enters the correct process;

$Case3$: If HR_c is not in the range of $(HR_p - 0.2, HR_p + 0.2)$ and A_c is in the

range of $(0.3 * A_p, 3 * A_p)$, then

$$HR_{correct} = \begin{cases} HR_p + \varepsilon & if HR_c - HR_p \geq 0.2 \\ HR_p - \varepsilon & if HR_c - HRp \leq -0.2 \\ HR_p & otherwise \end{cases} \tag{4.5}$$

Here, ε , the frequency correction, could be any small positive quantity, such as 0.1; and

$Case4$: If HR_c and A_c are not in range, the second closest cluster to the previous estimation in the Frequency-S domain is selected as the possible heartbeat cluster.

In reality, the assumption in $Case2$ is not always valid. The setting of the amplitude check is to avoid the emergence of some extreme situations. For example, the interference component caused by a certain random motion is decomposed into multiple parts. Furthermore, the frequency of a certain component is similar to the heartbeat frequency and is additionally stable. In $Case3$, we took precautions against possible detection failures, and estimated the results in this period to prevent any false detections in this period from affecting all results in the future.

The fact the cluster center is close to the heartbeat estimation does not imply that the cluster contains heartbeat components. There is a possibility that all the components do not come from the heartbeat, but the cluster center is very close to the previous estimation. One of the solutions of this problem is to set the number of clusters as large as possible. If there are enough classifications, the number of components in each category is smaller, and the cluster centers can better reflect the attributes of the members. Second, $Case4$ is also set to correspond to this situation.

The method used in this paper is not irreplaceable. EMD can replace SSA, and sparse signal reconstruction [36] can replace the final FFT. Many parameters in this

paper's algorithm are optimized after repeated trials, such as time window length, sampling rate, and the number of clusters.

4.4 Experiment of ASSA

In the experiment, a Texas Instrument (TI) mm-wave radar (IWR6843) operating from 60 to 64 GHz is employed. The maximal wavelength (at the 60 GHz band) is 4.99 mm. The frame period is 40 ms, and there are 128 chirps per frame. The sampling rate is 256 times per chirp. The subject's hand is also equipped with a wireless photoplethysmogram (PPG) device to record the heart rate for reference. Fig. 4.3 presents the initial scene-setting for the experiment. The distance between the subject and radar is 100 cm and is increased at a step of 10 cm until reaching 180 cm. Two subjects at each distance conducted three experiments, and the length of data collected in each experiment is 25 s. Each experiment is repeated ten times.

The experiment was divided into three groups. In the first group, the subject remained still, leant back into the chair, and tried to hold their breathing. This is simulating the situation when people is in working or sleeping. In the second group, the subject was asked to breathe as heavily as possible without leaning their backs on the back of the chair. In the third group, the subject was asked not to lean on the back of the chair while their upper body swayed randomly. This would cause the most interference and is one of the most challenging heartbeat extraction tasks for people in a sitting position.

Signals in three groups after processing are shown in Fig. 4.4, where each subfigure is for one. In Fig. 4.4a, the initial two-second oscillation is due to the subject's movement, and the signal is more stable afterwards. Fig.4.4b is from the second group. It is evident that the signal amplitude is much stronger than that of the previous group. Because the subject does not lean back on the chair while breathing heavily, the body is not in a stable position. The increased magnitude indicates

Figure 4.3 : Scene setup for experiment.

that the subject is slightly moving closer to the radar in this particular experiment. Fig. 4.4c demonstrates the signals for third group. The amplitude is larger than the previous groups and is mainly triggered by the movement of the upper body.

After construction, decomposition, and reconstruction, the signal enters the clustering step. Fig. 4.5a and Fig. 4.5b show the clustering of group 1 and group 3. The component feature values contained in group 3 are much larger than the threshold values of group 1. The red dot in the figure denotes the heartbeat group.

Fig. 4.6 shows the comparison of the selected cluster with the reference signal in the frequency domain. The three picture shows different conditions used with the three subfigures (Fig.4.6a: keeping still, Fig. 4.6b: heavy breath and Fig. 4.6c: subject with RBM). Four clustering methods are used here (K-means, Hierarchical, Mean-shift, and EM based on K-means). Among them, the results of EM and K-means are often the same. The clustering result of K-means is used in EM as its initial value, and the result of K-means is often already locally convergent. In Fig. 4.6a, the results of all clustering methods are the same and are also very close to the reference heart rate. In Fig. 4.6b and Fig. 4.6c, only the results of mean-shift clustering are close to the reference value, and other methods choose disturbing components as the heartbeat component. The advantage of the adaptiveness of mean-shift clustering is shown. This adaptability implies that the number of categories does not need to be manually selected, while the categories are manually chosen. Given that the number of cluster categories required for signals with interference and without interference is quite different, it is difficult to set several cluster categories that vary with the situation.

Finally, we compare the performance of several different methods and present the results in Fig. 4.7. The solid curve is for the wireless PPG device worn on the tester's left hand, and the dotted lines are for different clustering methods. Multiple Singular Spectrum Analysis (MSSA) and SSA methods are used for comparison. Over the time period, the test subject kept moving their upper body. The the mean-shift algorithm clustering achieves performance close to the PPG reference data, and the estimates gradually deviate from the real values when other clustering algorithms are used. The deviation increased with time. This is because the wrong estimations caused by incorrect clustering will also affect the next estimation. Additionally, both MSSA and SSA deviate considerably from the real values, demonstrating that our proposed method is robust to the RBM interference.

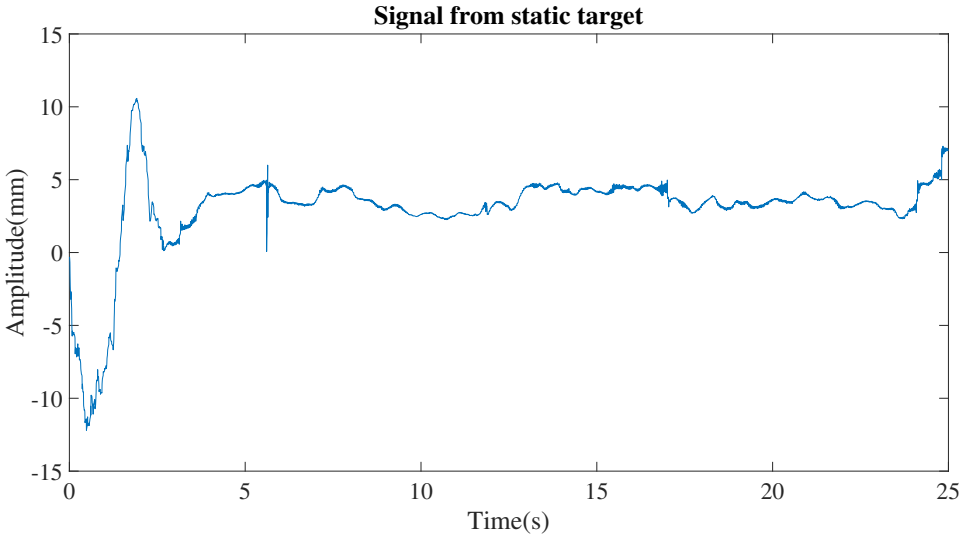

(a) Keep still

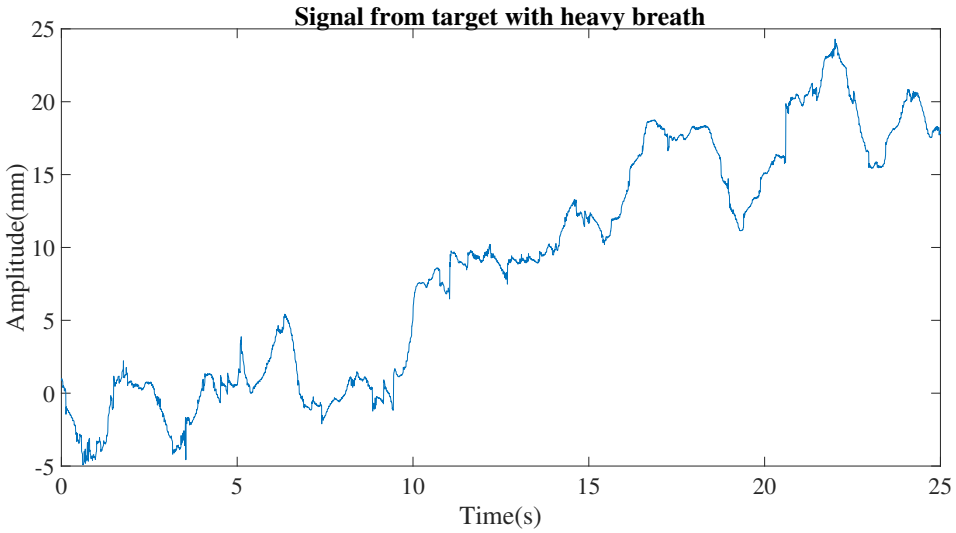

(b) With heavy breath

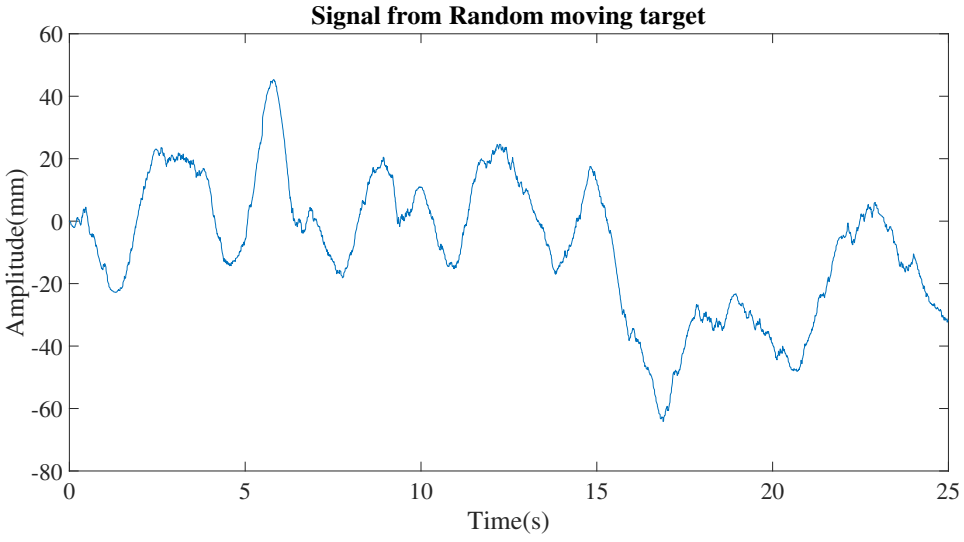

(c) With RBM

Figure 4.4 : Signal from different groups in experiment

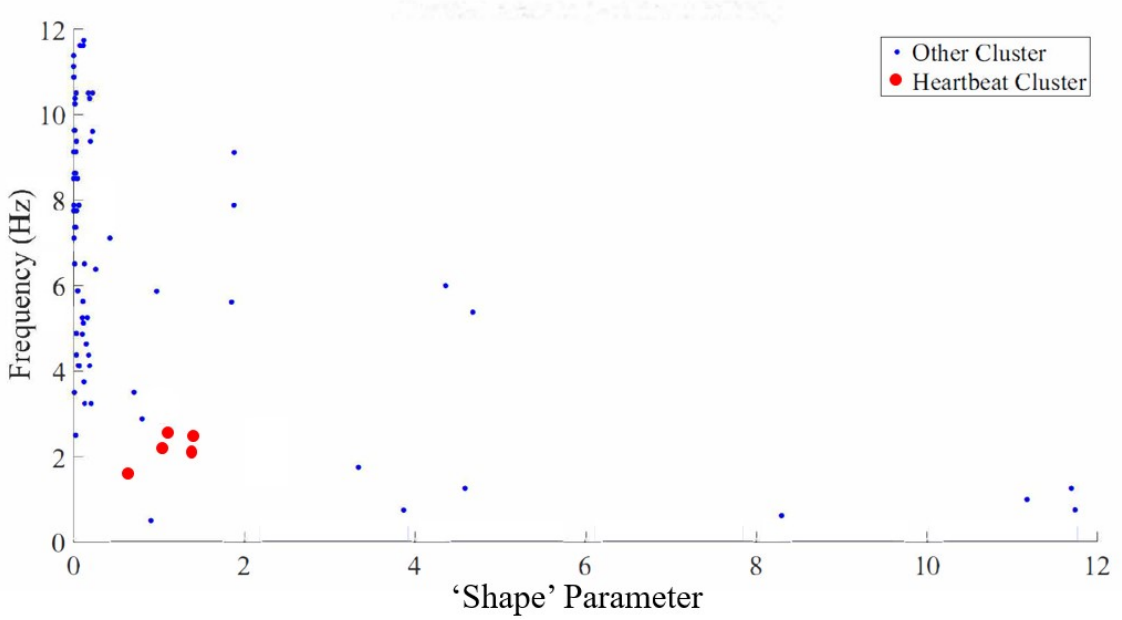

(a) Cluster of components (without RBM)

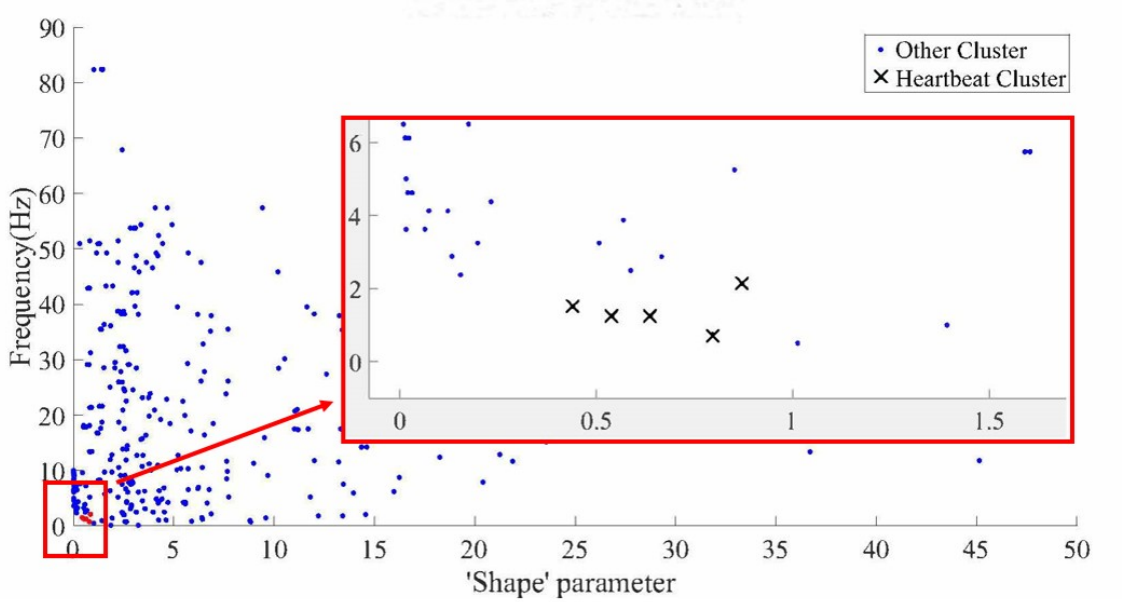

(b) Cluster of components (with RBM)

Figure 4.5 : Cluster of components in reconstructed signal

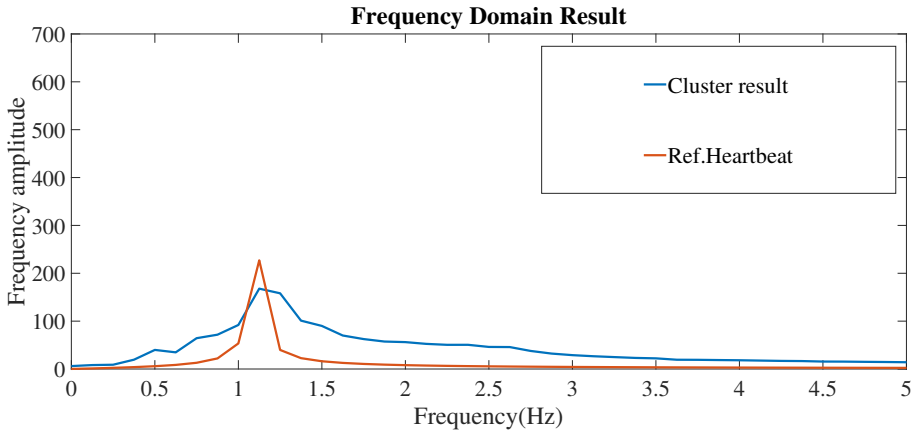

(a) Chosen cluster on Frequency domain (keep still)

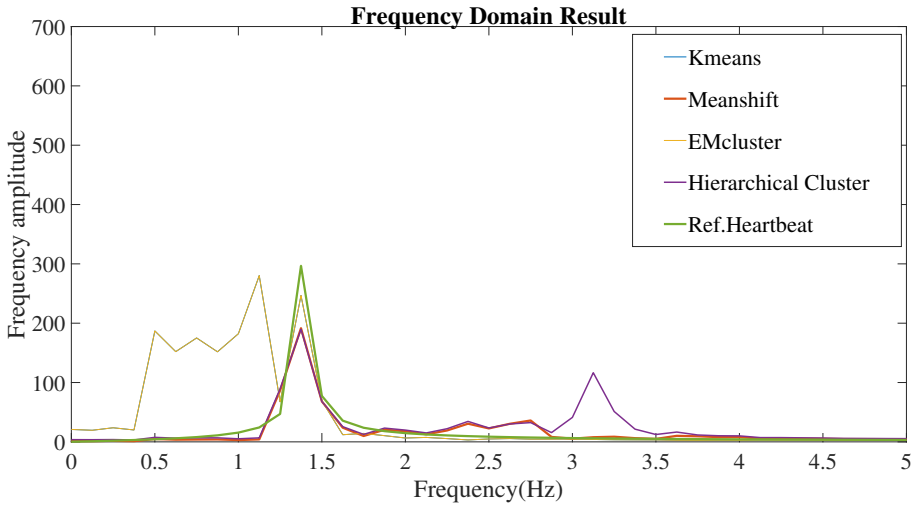

(b) Chosen cluster on Frequency domain (with heavy breath)

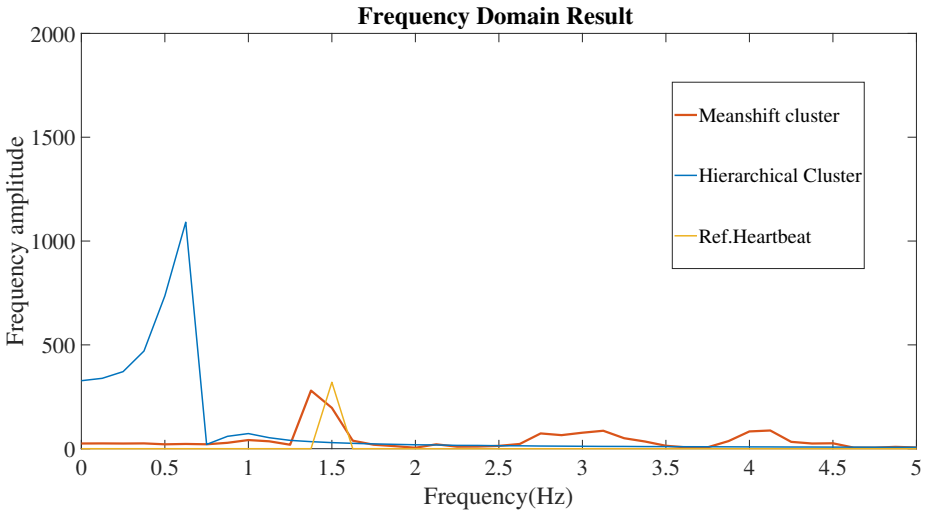

(c) Chosen cluster on Frequency domain (with RBM)

Figure 4.6 : Chosen cluster in Frequency domain

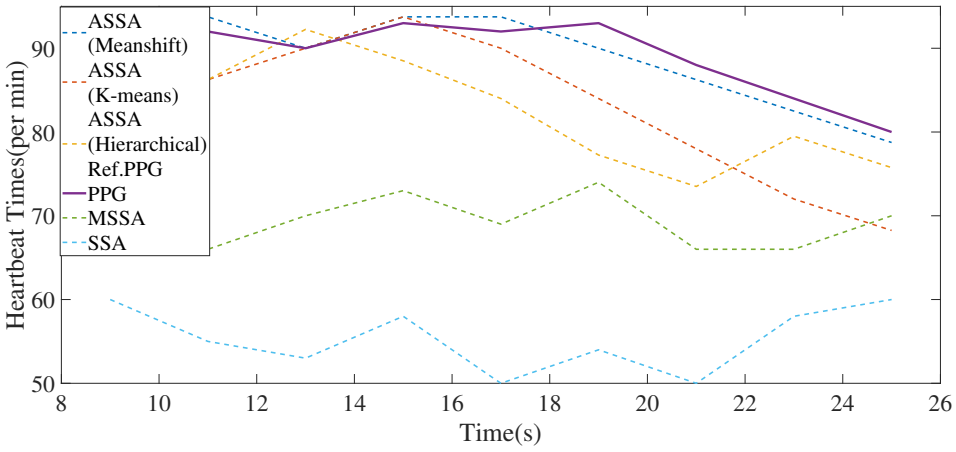

Figure 4.7 : Heartbeat Times(per minute) with different processing methods

Chapter 5

Conclusion

5.1 Conclusion

In this thesis, the first work uses the GMM to model the noise to obtain better heartbeat detection accuracy, and the second work adopts Advanced SSA for extracting heartbeat components from the target with RBM. In this thesis's first work, we used the GMM-CSC framework, which has not been utilized in heartbeat detection before, for individual heartbeat recognition. First, DC compensation and phase unwrapping are used to preprocess the data. We use GMM to model the noise and use the EM algorithm to update the parameters. The M-step can be transformed into a CSC problem and, in order to improve the operation speed, we use APG to optimize. Simulations and experiments based on this algorithm are carried out, and the results indicate that the proposed scheme can achieve the expected purpose of de-noising and heart rate extraction. In the second work of this thesis, we use a variety of clustering methods to enhance SSA so that it can better extract the heartbeat signal and remove the movement and respiratory components. In this process, the adaptive mean shift clustering method offers the best performance. The mean shift enhanced algorithm can detect the heartbeat of the upper body moving randomly.

Generally speaking, the first work has a better performance in a complex environment, such as an environment with problematic noise interference, but not good at dealing with RBM. The second algorithm can more effectively deal with the interference of accidental upper body movement. The second algorithm has a broader

application prospect in real life. For example, remote heartbeat detection for people sitting on chairs in a work setting. Of course, remote heartbeat detection still faces significant challenges, its accuracy does not meet the medical requirements, and there is still a lack of algorithm to accurately extract QRS waveform in the ECG signal. QRS waveform is an essential basis for medical diagnosis.

5.2 Future work

The work undertaken in this paper can be further expanded in the future.

First, the CSC algorithm based on GMM is still relatively rough. The source of this algorithm is the early image denoising technology. Although the performance of the heartbeat extraction technology is acceptable in this framework, there is still much room for development.

Secondly, in the heartbeat extraction algorithm based on clustering, the clustering parameters selected in this paper may not be the best choice. In addition, regardless of the problem of restoring the original signal, clustering algorithms in the time - frequency domain may have better results.

In fact, the existing remote heartbeat detection methods can not obtain the heartbeat information of the moving target. Additional prior information seems to be necessary. In addition, any blocking will bring huge performance loss. These are the focus of future research.

Bibliography

[1] P. Wang, F. Qi, M. Liu, F. Liang, H. Xue, Y. Zhang, H. Lv, and J. Wang, "Non-contact heart rate measurement based on an improved convolutional sparse coding method using ir-uwb radar," *IEEE Access*, vol. 7, pp. 158 492–158 502, 2019.

[2] C. Li and J. Lin, "Optimal carrier frequency of non-contact vital sign detectors," in *2007 IEEE Radio and Wireless Symposium*. IEEE, 2007, pp. 281–284.

[3] K.-M. Chen, Y. Huang, J. Zhang, and A. Norman, "Microwave life-detection systems for searching human subjects under earthquake rubble or behind barrier," *IEEE transactions on biomedical engineering*, vol. 47, no. 1, pp. 105–114, 2000.

[4] D. T. Petkie, C. Benton, and E. Bryan, "Millimeter wave radar for remote measurement of vital signs," in *2009 IEEE Radar Conference*. IEEE, 2009, pp. 1–3.

[5] H.-R. Chuang, H.-C. Kuo, F.-L. Lin, T.-H. Huang, C.-S. Kuo, and Y.-W. Ou, "60-ghz millimeter-wave life detection system (mlds) for noncontact human vital-signal monitoring," *IEEE Sensors Journal*, vol. 12, no. 3, pp. 602–609, 2011.

[6] S. Bakhtiari, T. W. Elmer, N. M. Cox, N. Gopalsami, A. C. Raptis, S. Liao, I. Mikhelson, and A. V. Sahakian, "Compact millimeter-wave sensor for remote monitoring of vital signs," *IEEE Transactions on Instrumentation and Measurement*, vol. 61, no. 3, pp. 830–841, 2011.

[7] B.-K. Park, O. Boric-Lubecke, and V. M. Lubecke, "Arctangent demodulation with dc offset compensation in quadrature doppler radar receiver systems," *IEEE transactions on Microwave theory and techniques*, vol. 55, no. 5, pp. 1073–1079, 2007.

[8] M. Budge and M. Burt, "Range correlation effects on phase and amplitude noise," in *Proceedings of Southeastcon'93*. IEEE, 1993, pp. 5–p.

[9] M. Brink, C. H. Müller, and C. Schierz, "Contact-free measurement of heart rate, respiration rate, and body movements during sleep," *Behavior research methods*, vol. 38, no. 3, pp. 511–521, 2006.

[10] A. D. Droitcour, O. Boric-Lubecke, V. M. Lubecke, J. Lin, and G. T. Kovacs, "Range correlation and i/q performance benefits in single-chip silicon doppler radars for noncontact cardiopulmonary monitoring," *IEEE Transactions on Microwave Theory and Techniques*, vol. 52, no. 3, pp. 838–848, 2004.

[11] N. Maaref, P. Millot, C. Pichot, and O. Picon, "A study of uwb fm-cw radar for the detection of human beings in motion inside a building," *IEEE Transactions on Geoscience and Remote Sensing*, vol. 47, no. 5, pp. 1297–1300, 2009.

[12] T. Mitomo, N. Ono, H. Hoshino, Y. Yoshihara, O. Watanabe, and I. Seto, "A 77 ghz 90 nm cmos transceiver for fmcw radar applications," *IEEE journal of solid-state circuits*, vol. 45, no. 4, pp. 928–937, 2010.

[13] A. G. Stove, "Linear fmcw radar techniques," in *IEE Proceedings F (Radar and Signal Processing)*, vol. 139, no. 5. IET, 1992, pp. 343–350.

[14] C. Gu and C. Li, "Dc coupled cw radar sensor using fine-tuning adaptive feedback loop," *Electronics letters*, vol. 48, no. 6, pp. 344–345, 2012.

[15] X. Zhao, C. Song, V. Lubecke, and O. Boric-Lubecke, "Dc coupled doppler radar physiological monitor," in *2011 Annual International Conference of the*

IEEE Engineering in Medicine and Biology Society. IEEE, 2011, pp. 1909–1912.

[16] J. Salmi, O. Luukkonen, and V. Koivunen, "Continuous wave radar based vital sign estimation: Modeling and experiments," in *2012 IEEE Radar Conference*. IEEE, 2012, pp. 0564–0569.

[17] C. Ye, K. Toyoda, and T. Ohtsuki, "Blind source separation on non-contact heartbeat detection by non-negative matrix factorization algorithms," *IEEE Transactions on Biomedical Engineering*, vol. 67, no. 2, pp. 482–494, 2019.

[18] J. C. Lin, "Noninvasive microwave measurement of respiration," *Proceedings of the IEEE*, vol. 63, no. 10, pp. 1530–1530, 1975.

[19] C. Gu, G. Wang, Y. Li, T. Inoue, and C. Li, "A hybrid radar-camera sensing system with phase compensation for random body movement cancellation in doppler vital sign detection," *IEEE Transactions on Microwave Theory and Techniques*, vol. 61, no. 12, pp. 4678–4688, 2013.

[20] C. Gu, G. Wang, T. Inoue, and C. Li, "Doppler radar vital sign detection with random body movement cancellation based on adaptive phase compensation," in *2013 IEEE MTT-S International Microwave Symposium Digest (MTT)*. IEEE, 2013, pp. 1–3.

[21] B. S. Kim and S. K. Yoo, "Motion artifact reduction in photoplethysmography using independent component analysis," *IEEE transactions on biomedical engineering*, vol. 53, no. 3, pp. 566–568, 2006.

[22] Z. Zhang, Z. Pi, and B. Liu, "Troika: A general framework for heart rate monitoring using wrist-type photoplethysmographic signals during intensive physical exercise," *IEEE Transactions on biomedical engineering*, vol. 62, no. 2, pp. 522–531, 2014.

[23] I. Mostafanezhad, E. Yavari, O. Boric-Lubecke, V. M. Lubecke, and D. P. Mandic, "Cancellation of unwanted doppler radar sensor motion using empirical mode decomposition," *IEEE Sensors Journal*, vol. 13, no. 5, pp. 1897–1904, 2013.

[24] I. V. Mikhelson, S. Bakhtiari, T. W. Elmer, A. V. Sahakian *et al.*, "Remote sensing of heart rate and patterns of respiration on a stationary subject using 94-ghz millimeter-wave interferometry," *IEEE Transactions on Biomedical Engineering*, vol. 58, no. 6, pp. 1671–1677, 2011.

[25] M. R. Ram, K. V. Madhav, E. H. Krishna, N. R. Komalla, and K. A. Reddy, "A novel approach for motion artifact reduction in ppg signals based on as-lms adaptive filter," *IEEE Transactions on Instrumentation and Measurement*, vol. 61, no. 5, pp. 1445–1457, 2011.

[26] R. Yousefi, M. Nourani, S. Ostadabbas, and I. Panahi, "A motion-tolerant adaptive algorithm for wearable photoplethysmographic biosensors," *IEEE journal of biomedical and health informatics*, vol. 18, no. 2, pp. 670–681, 2013.

[27] Y. Wang, J. T. Kwok, and L. M. Ni, "Generalized convolutional sparse coding with unknown noise," *IEEE Transactions on Image Processing*, vol. 29, pp. 5386–5395, 2020.

[28] M. Alizadeh, G. Shaker, J. C. M. D. Almeida, P. P. Morita, and S. Safavi-Naeini, "Remote monitoring of human vital signs using mm-wave fmcw radar," *IEEE Access*, vol. 7, pp. 54 958–54 968, 2019.

[29] Q. Yao, J. T. Kwok, F. Gao, W. Chen, and T.-Y. Liu, "Efficient inexact proximal gradient algorithm for nonconvex problems," *arXiv preprint arXiv:1612.09069*, 2016.

[30] Y. Wang, J. T. Kwok, and L. M. Ni, "Generalized convolutional sparse coding with unknown noise," *IEEE Transactions on Image Processing*, vol. 29, pp. 5386–5395, 2020.

[31] H. Shen, C. Xu, Y. Yang, L. Sun, Z. Cai, L. Bai, E. Clancy, and X. Huang, "Respiration and heartbeat rates measurement based on autocorrelation using ir-uwb radar," *IEEE Transactions on Circuits and Systems II: Express Briefs*, vol. 65, no. 10, pp. 1470–1474, 2018.

[32] S. Wang, A. Pohl, T. Jaeschke, M. Czaplik, M. Köny, S. Leonhardt, and N. Pohl, "A novel ultra-wideband 80 ghz fmcw radar system for contactless monitoring of vital signs," in *2015 37th Annual International Conference of the IEEE Engineering in Medicine and Biology Society (EMBC)*. IEEE, 2015, pp. 4978–4981.

[33] R. Krishnan, B. Natarajan, and S. Warren, "Two-stage approach for detection and reduction of motion artifacts in photoplethysmographic data," *IEEE transactions on biomedical engineering*, vol. 57, no. 8, pp. 1867–1876, 2010.

[34] M. Le, D.-K. Le, and J. Lee, "Multivariate singular spectral analysis for heartbeat extraction in remote sensing of uwb impulse radar," *Sensors and Actuators A: Physical*, p. 111968, 2020.

[35] S. Kazemi, A. Ghorbani, H. Amindavar, and C. Li, "Cyclostationary approach to doppler radar heart and respiration rates monitoring with body motion cancelation using radar doppler system," *Biomedical Signal Processing and Control*, vol. 13, pp. 79–88, 2014.

[36] I. F. Gorodnitsky and B. D. Rao, "Sparse signal reconstruction from limited data using focuss: A re-weighted minimum norm algorithm," *IEEE Transactions on signal processing*, vol. 45, no. 3, pp. 600–616, 1997.

[37] F.Zhu and K.Wu, "Doppler Radar Techniques for Vital Signs Detection Featuring Noise Cancellation" *IEEE Transactions on signal processing, vol* vol. 45, no. 3, pp. 897–903, 2019